Reducing the electric field sensitivity of a Rydberg state transition by the application of a non-resonant microwave field

by

Lucas Jones

A thesis
presented to the University of Waterloo
in fulfillment of the
thesis requirement for the degree of
Master of Science
in
Physics

Waterloo, Ontario, Canada, 2012

I hereby declare that I am the sole author of this thesis. This is a true copy of the thesis, including any required final revisions, as accepted by my examiners.

I understand that my thesis may be made electronically available to the public.

Lucas Jones

Abstract

The ^{87}Rb $49s_{1/2} \rightarrow 48s_{1/2}$ Rydberg state transition was rendered insensitive to electric field fluctuations about a 1 V/cm dc electric field. This was accomplished by applying a non-resonant 38.445 GHz microwave field to modify the electric dipole moment difference between the two states involved. This effect can be used to preserve the coherence of Rydberg state qubits in the presence of varying electric fields.

Acknowledgements

This work would not have been possible without the help and support of many people. First of all I would like to thank my supervisor Jim Martin, for teaching me so much and helping me perform these experiments. The work you have done and the potential you have created in this group is truly increadible.

I would like to thank those who have helped by loaning equipment and resources. Professors Jan Kycia and David Cory supplied us with various microwave components. Professor Rafaat Mansour provided us with access to finite element simulation software.

Thank you to the members of my advisory and examining comittee, Dr. Joseph Sanderson, Dr. Kevin Resch, Dr. Wing-Ki Liu and Dr. David Cory, for your suggestions and support.

I would also like to thank Harmon Vander Heide, Peter Kessel, Hiruy Haile, Michael Lang, Andrew Dube, Jacek Szubra, Krunomir Dvorski and Zhenwen Wang - my friends in the machine shop and electronics shop - for teaching me so much and helping me solve so many problems.

I would like to thank all of my fellow students in our research group; Jeff Carter, Chelsea Liekhus-Schmaltz, Parisa Bohlouli-Zanjani, Mike Mazurek and Mozhgan Torabifard. Our conversations were invaluable, whether they were for passing knowledge, or exposing new perspectives. Most valuable of all, you have shared with me your passion for our work.

Contents

List of Figures

Chapter 1

Introduction

1.1 Motivation

Atoms excited to Rydberg states are a promising candidate for storing quantum information, owing to their long radiative lifetimes [2]. The polarizability of Rydberg atoms scales as n^7 [2] where n is the principal quantum number. This scaling amplifies the electric field sensitivity of Rydberg atoms, reducing coherence times compared to lower n states. This effect is compounded in the presence of a non-zero electric field [1][5], since the states will inevitably have different electric dipole moments giving the transition frequency a first order dependance on the electric field (Fig.1.1). The goal of this work is to demonstrate a method for eliminating the sensitivity to deviations about a non-zero electric field. Our method involves applying a non-resonant microwave dressing field to modify the dipole moments of the two states such

that they match.

Using perturbation theory, we can gain insight into the effect of the detuned dressing field and determine how much power is required. Floquet theory [13] is used to solve for the energies of the system.

This work is similar to a proposal by Hyafil *et al.* [5] in which atoms are to be excited to circular Rydberg states and held in a dynamic trap. These states can have lifetimes on the order of milliseconds [4][3]. To preserve the population of circular states, a dc electric field is required to split the degeneracy between the circular states and lower angular momentum states. The dc electric field introduces different dipole moments for the two circular states, which leads to limited coherence time for atoms due to fluctuations of the electric field. To remedy this, they propose applying a non-resonant microwave field to eliminate the difference in the dipole moments.

In this work we have addressed some of the difficulties involved in using non-resonant microwave fields to null dipole moment differences. One such difficulty is the strong influence of ellipticity of the dressing microwaves. We hypothesize that ellipticity results in spectral line splitting which will be discussed in chapter 3. Another consideration is the noise spectral density of the dressing microwave source, which can cause broadening of spectral lines as discussed in chapter 4.

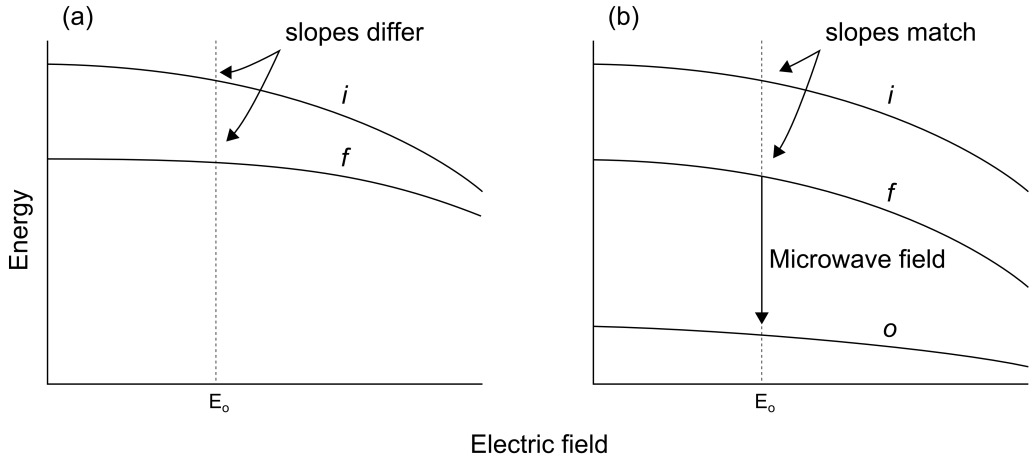

Figure 1.1: An exaggerated schematic of the experiment. For non-dressed states (a), the dipole moments are different at E_o. The dipole moment of state f can be modified (b) by coupling to a third state o using a non-resonant *dressing* microwave field.

Chapter 2

Apparatus and experimental techniques

To demonstrate the nulling of the dipole moment difference between Rydberg states, we work with a cooled cloud of ^{87}Rb atoms held in a magneto-optical trap (MOT) [10]. The MOT consists of a stainless steel vacuum chamber maintained at 10^{-8} Torr, lasers which apply a velocity dependent force to the atoms and an Anti-Helmholtz coil (AHC) pair which makes the laser radiation pressure position dependant.

The apparatus used for this work was available from previous experiments [1], however the source of Rb had been depleted. To replace the Rb source, it was necessary to vent the vacuum system and realign the optics. Modifications to the laser locking system were implemented, as well as many other modifications through the course of the experiment. All of these modifica-

tions and methods are described in the following sections.

2.1 Magneto-optical trap

Six laser beams intersect orthogonally on three axes at the center of a vacuum chamber (Figs.2.11, 2.12)[10]. The wavelength of these beams is red detuned by approximately 10 MHz from the ^{87}Rb $5s_{1/2}, F = 2 \rightarrow 5p_{3/2}, F = 3$ transition such that atoms with particular velocities experience radiation pressure from the Doppler shifted laser beams. In this configuration, the atoms are said to be in *optical molasses*, since the motion of atoms is slowed. To trap the atoms, it is necessary to apply a position dependant force, since the atoms would otherwise be able to drift out of the optical molasses. The same laser radiation pressure responsible for optical molasses can be made position dependant if the beam polarizations are properly configured, and a magnetic field applied. An anti-Helmholtz coil pair generates a magnetic quadrupole zero with a magnetic field amplitude that increases linearly with distance from the MOT center (See Fig.2.1 and Fig.2.2). Each laser beam axis has two counter-propagating and oppositely circularly polarized laser beams which are tuned below the zero field atomic transition frequency. Away from the quadrupole zero, the atoms are Zeeman shifted into resonance with one of the detuned *cooling and trapping* laser beams and are forced back towards the MOT center. The polarization of the CT beams, and the direction of the magnetic field ensures that the atoms are forced in the correct direction.

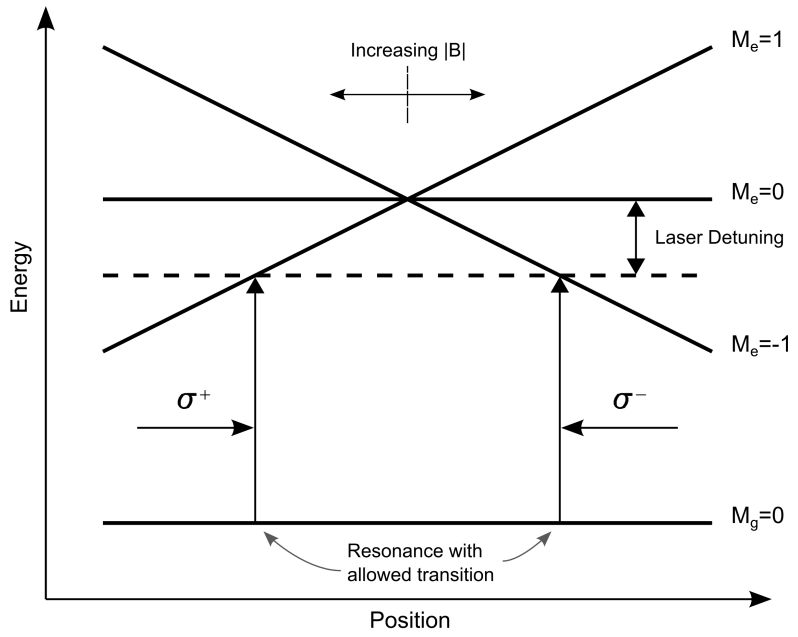

Figure 2.1: 1D laser cooling and trapping. Two laser beams detuned from an atomic transition and counter-propogating are oppositely circularly polarized. The magnetic field amplitude increases linearly with distance from a magnetic field zero, causing atomic transitions to be Zeeman shifted into resonance with the lasers. The resulting radiation pressure slows the atoms and traps them near the magnetic field zero.

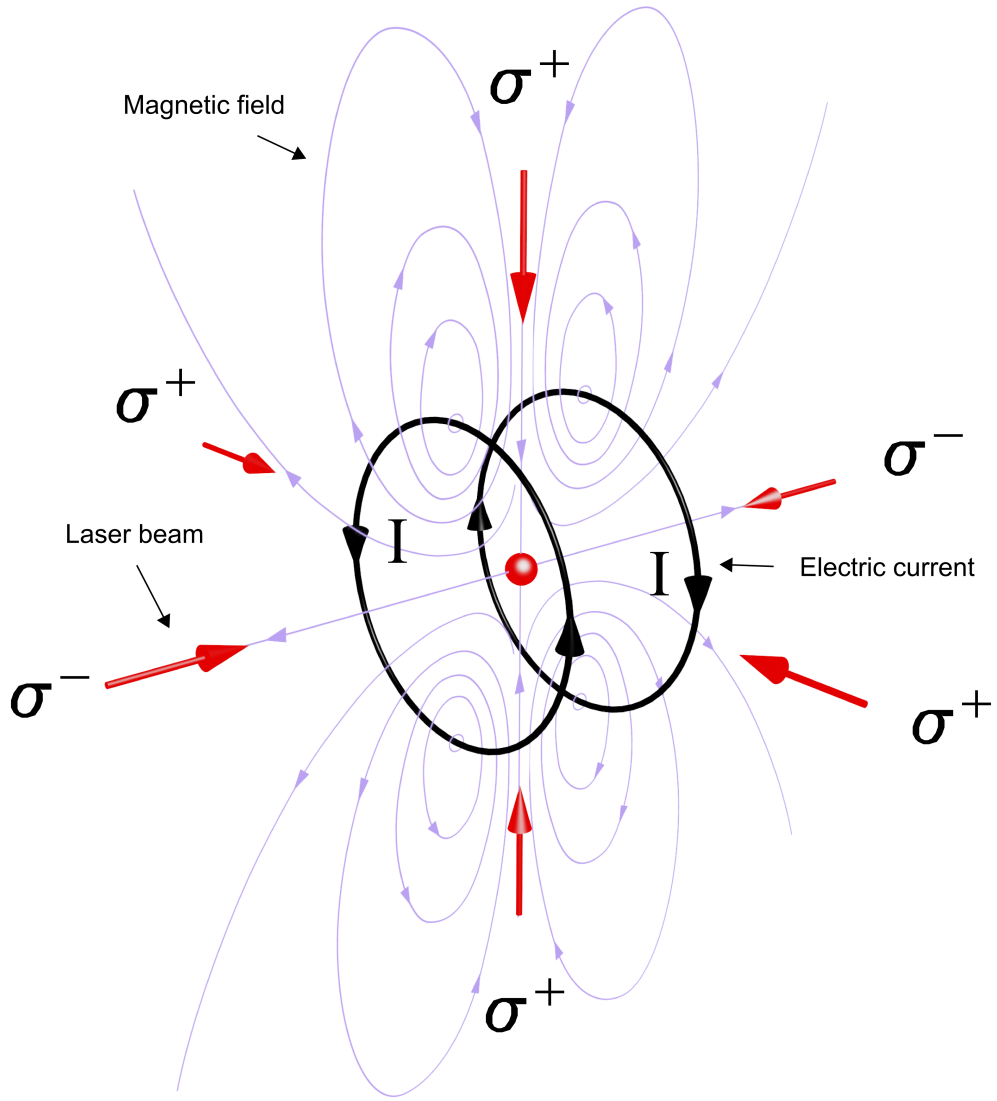

Figure 2.2: Laser cooling and trapping. A magnetic quadrupole zero is generated by an AHC pair. Three pairs of collinear and counter-propogating laser beams cause velocity and position dependant forces, which slow and trap atoms.

The $5s_{1/2}$ state has two hyperfine sublevels: F=1 and F=2 (Fig.2.3). The detuned CT laser beams can cause Raman scattering from $5p_{3/2}, F = 3$ to the $5s_{1/2}, F = 1$ ground state. In this state, the CT laser cannot interact with the atom, allowing it to escape from the trap. To re-trap the atom, a second laser frequency is applied which drives the $5s_{1/2}, F = 1 \rightarrow 5p_{3/2}, F = 2$ transition. Once in the $5p_{3/2}, F = 2$ state, the atom can decay back to the $5s_{1/2}, F = 2$ state and become trapped once again. Without this *repump* laser beam, the atoms would quickly accumulate in the $5s_{1/2}, F = 2$ ground state and the steady state population of the trap would be too low for the purposes of the experiment.

2.2 Vacuum chamber

The MOT must be operated in a vacuum to reduce collisions between trapped atoms and background molecules. Figure 2.4 shows the vacuum chamber at the center of the Helmholtz and anti-Helmholtz coils.

Rb is released into the vacuum chamber from metal containers filled with a Rb bearing chemical. There are two parallel banks of these Rb dispensers, which offgas as the chemical is heated. The dispensers are mounted on a ø2.75" CF flange with electrical feed-throughs, which allow the Rb dispensers to be resitively heated. To replace this flange, it is necessary to vent the vacuum chamber to atmospheric pressure, however precautions need to be taken to ensure water vapour does not contaminate the vacuum chamber

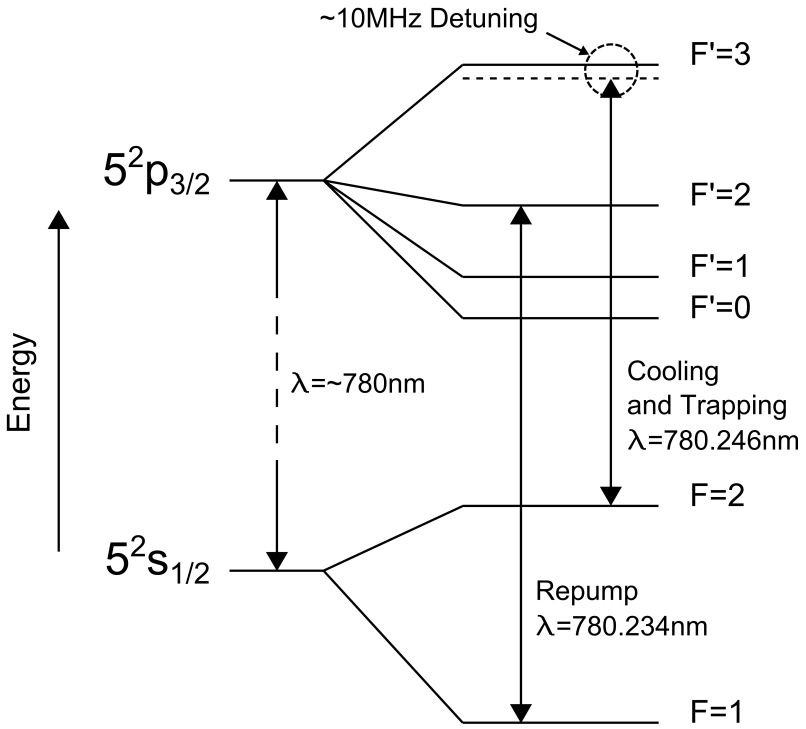

Figure 2.3: The ^{87}Rb Energy levels involved in cooling and trapping. Two laser beams are required for cooling and trapping: the *repump* laser is tuned to the $5s_{1/2}, F = 1 \rightarrow 5p_{3/2}, F = 2$ transition, and the CT laser detuned approximately 10 MHz below the $5s_{1/2}, F = 2 \rightarrow 5p_{3/2}, F = 3$ transition. The repump laser is responsible for evacuating the $5s_{1/2}, F = 1$ ground state, and the CT laser causes the position and velocity dependant forces which slow and trap the atoms.

during this operation. One way to prevent backflow of air into the vacuum chamber when removing the Rb dispenser is to fill the chamber with heated N_2, and ensure that the N_2 continuously flows out of the open flange. The N_2 is heated such that any water content present is less likely to condense on the vacuum chamber surfaces.

Reducing the pressure inside the vacuum chamber requires a three stage pumping procedure. First, a blower pump provides a rough vacuum of several Torr. Next, a two chamber sorption pump reduces the pressure from several Torr to several milliTorr. The final stage is an ion pump (Duniway triode sputter-ion pump, RVA-20-TR/M) which is able to reach the required pressure for operating a MOT. The minimum vacuum chamber pressure is limited by the offgassing rate of the stainless steel walls, as well as any components installed within the chamber. To reduce the amount of offgassing, it is necessary to thoroughly clean the components prior to assembly. The components are first cleaned with liquid detergent in an ultrasonic cleaner for at least a half hour. The parts are then cleaned in trichloroethylene for another half hour in the ultrasonic cleaner, and rinsed with HPLC grade methanol. Even with thorough cleaning, the offgassing of components and vacuum chamber walls limits the minimum pressure to roughly 10^{-7} Torr. Heating the vacuum chamber while the ion pump is running accelerates offgassing, and allows molecules bound to surfaces to be captured by the ion pump. Leaving the system at an elevated temperature for an extended period of time makes it possible to reach a lower pressure when the system is

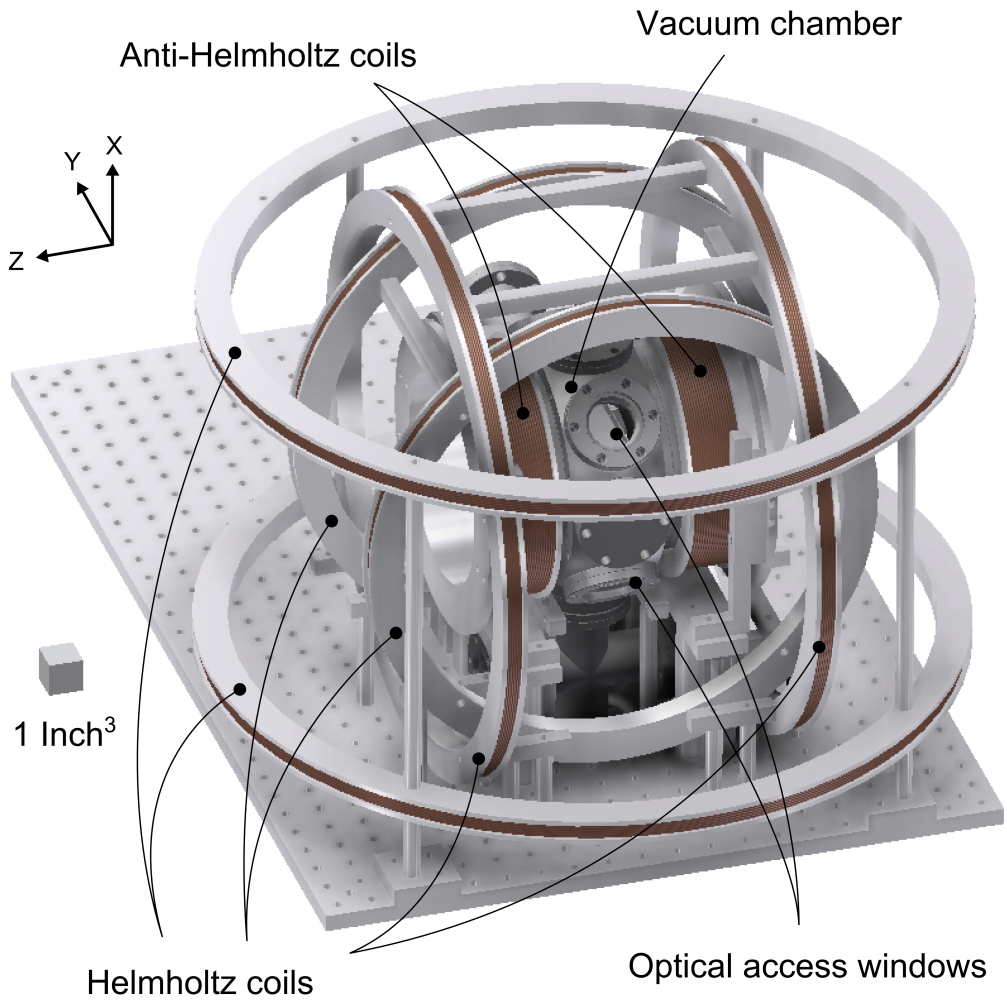

Figure 2.4: The vacuum chamber including Helmholtz and anti-Helmholtz coils.

returned to room temperature. For our purposes, we found that heating the chamber to 100°C for 20 hours reduced the pressure sufficiently. The final pressure was 10^{-9} Torr as read from an ion-gauge.

2.3 Laser stabilization

The lasers used to produce the cooling and trapping as well as repump beams are susceptible to temperature drift, mechanical vibrations and other influences in the lab environment. The lasers can be locked relative to an atomic transition to achieve the necessary stability. For this experiment, a laser is stabilized relative to the ^{87}Rb $5s_{1/2}, F = 1 \rightarrow 5p_{3/2}, F = 1$ transition. This stabilized laser also acts as the source for the repump beam. To generate the frequency error signal necessary to stabilize the repump laser, a technique called frequency modulated saturated absorption spectroscopy (FMSAS) is used [6]. Once stabilized, the repump laser acts as a reference for the cooling and trapping laser. Stability is transferred from the repump laser to the CT laser using a technique called beat note locking, which allows control of the frequency difference between the lasers.

Like the repump and CT lasers, the Ti:Sapphire laser which is responsible for producing the *Rydberg excitation* beam also requires external stabilization. A transfer cavity serves this purpose and is in turn stabilized relative to the repump laser. These experimental techniques are explained in the following sections.

2.3.1 FM saturated absorption spectroscopy

FMSAS is a technique used to generate a signal which indicates whether the frequency of a laser frequency is above or below an atomic spectral line [6]. the FMSAS signal can be used to stabilize the laser frequency relative to the spectral line. This technique is an extension of a simpler technique called saturated absorption spectroscopy (SAS), and so an explanation of SAS is a useful first step in understanding FMSAS.

SAS involves splitting a laser beam into two parts, and passing these components through a vapour cell on collinear but counter-propagating paths (see Fig.2.6). The two beams are referred to as the pump and probe, with the pump beam having much more power than the probe. A photodiode detects the power of the probe beam after it has travelled through the vapour cell. The laser frequency can be scanned to show that the probe is absorbed for a range of frequencies near atomic resonances due to Doppler broadening from molecular motion. When the laser is detuned from any atomic resonance, the atoms which are Doppler shifted into resonance with the pump beam and probe beam are distinct, since they are traveling in opposite directions. When the laser is resonant with an atomic transition however, the high power pump beam will excite the atoms which would otherwise have absorbed the probe beam, causing a sharp reduction in probe beam absorption. These strong reductions in probe absorption also occur at frequencies *between* atomic resonances - called cross-over frequencies (See part a of Fig.2.5). What results is a spectrum where sharp dips in absorption - called Lamb dips - correspond

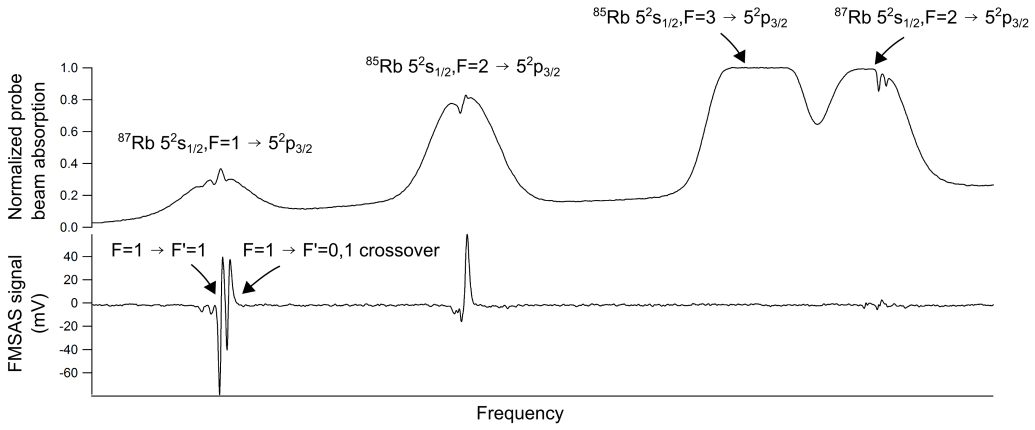

Figure 2.5: SAS spectrum for ^{87}Rb as well as the FMSAS output signal which can be used as an error signal for laser stabilization. The sharp reductions in absorption in the SAS spectrum represent either atomic transitions, or crossover frequencies between two atomic transitions.

to the atomic transition frequencies of stationary atoms.

FMSAS builds on this system, and is capable of generating a signal which indicates whether the laser frequency is higher or lower than the atomic transition frequency. This is done by modulating the frequency of the pump beam using an electro-optic modulator (EOM), which causes the absorption of the probe beam to modulate at the same frequency when the laser is near an atomic transition (see Fig.2.7). The probe beam photodiode signal can be demodulated using the same signal used to modulate the EOM. This requires the use of a fast photodiode, however a slow photodiode also detects the probe beam (Fig.2.6) to generate a SAS signal. The phase of the probe beam modulation with respect to the phase of the pump beam modulation depends to which side of the atomic transition the laser is detuned. As a

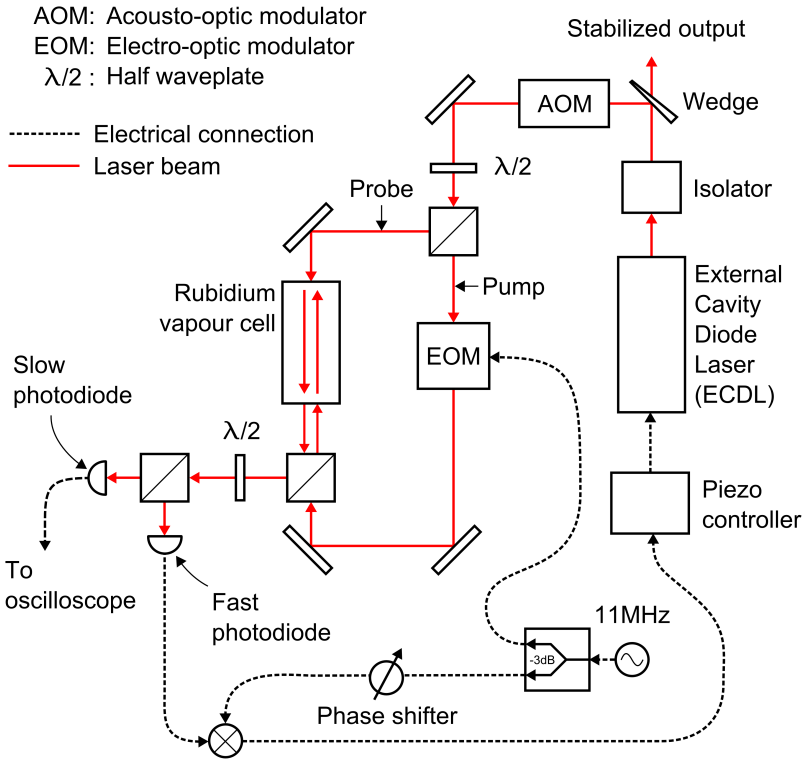

Figure 2.6: Schematic of a FM Saturated Absorption Spectroscopy system. The SAS spectrum can be observed using the slow photodiode signal. The FMSAS signal is obtained by mixing the output of the fast photodiode with the EOM modulation signal.

result, the polarity of the demodulated signal depends on whether the laser is red detuned or blue detuned from the atomic transition. This signal can be used as the error signal in a feedback loop to stabilize the laser frequency relative to the atomic transition.

At room temperature, the vapour pressure of the ^{87}Rb isotope is too low for FMSAS to yield a useable signal to lock the laser relative to the repump transition, or nearby transitions. By heating the vapour to 59°C, a strong

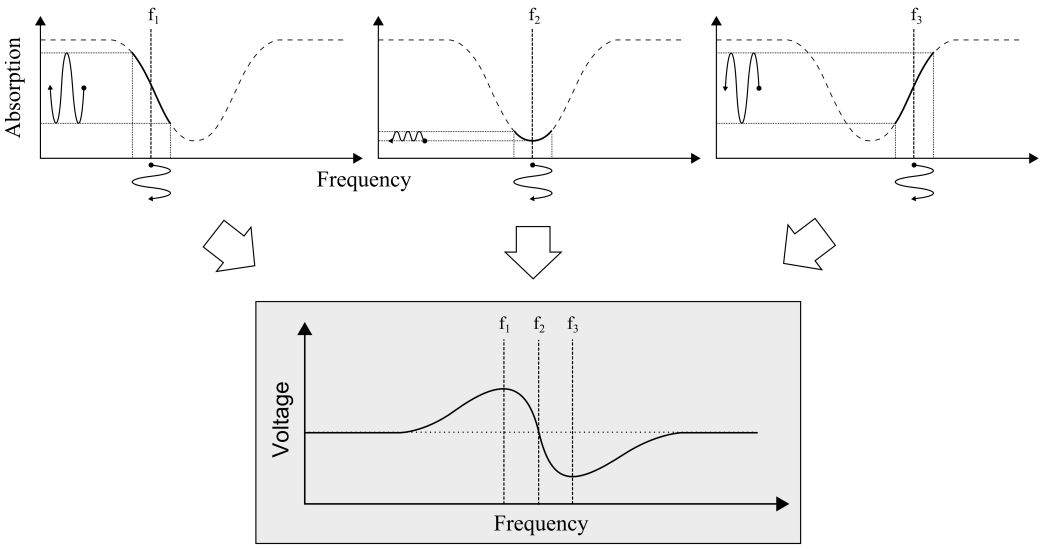

Figure 2.7: Mapping of pump beam frequency modulation to probe beam amplitude modulation in a FMSAS system (after Ref.[6]). The output of the FMSAS electronics generates a signal which indicates whether the frequency of a laser is above or below an atomic transition frequency.

FMSAS signal can be observed for the $5s_{1/2}, F = 1 \rightarrow 5p_{3/2}, F = 1$ transition, which is 157 MHz red detuned from the $5s_{1/2}, F = 1 \rightarrow 5p_{3/2}, F = 2$ repump transition [15]. In this experiment, an acousto-optic modulator (AOM) is be used to reduce the frequency of the laser beam by 80 MHz before entering the FMSAS system. A second AOM is used to increase the frequency of the laser beam which is sent to the vacuum chamber by 80 MHz. The combination of these two AOM shifts results in a laser beam which is 160 MHz higher than the atomic transition frequency used to lock the laser, and therefore only several MHz detuned from the repump transition. The repump transition has a linewidth of 10 MHz and is driven by the stabilized repump laser beam.

2.3.2 Beat-note locking

Beat note locking can be used to transfer the stability from one laser to a second laser if the difference between the laser frequencies is within a certain range. A good review of the method is given in Ref.[12]. This method involves heterodyning the two lasers on a detector, and using the resulting beat note signal to stabilize the frequency difference by controlling the wavelength of the unstable laser. The maximum frequency difference is limited by the bandwidth of the detector, which for relatively inexpensive and readily available detectors, sets a practical limit of a 10 GHz.

The cooling and trapping laser needs to be stabilized 10 MHz red detuned from the $5s_{1/2}, F = 2 \rightarrow 5p_{3/2}, F = 3$ transition. In this experiment, the repump beam which is 80 MHz blue shifted from the $5s_{1/2}, F = 1 \rightarrow 5p_{3/2}, F =$

2 transition is used as the reference (Fig.2.8). The frequency between the reference beam and CT beam is 6.421 GHz, which falls within the bandwidth of the detector. This beat note signal is then mixed with the output of a custom built synthesizer at 6.277 GHz, which yields a lower sideband frequency of 144 MHz. The upper sideband frequency is far above the bandwidth of the electronics and is attenuated. The 144 MHz signal is then mixed one more time using a voltage controlled oscillator which is tuned to 100 MHz.

The high frequency sideband is attenuated by a filter, resulting in a 44 MHz sine wave. This signal is divided between two transmission lines having a length difference of 15 feet, and which terminate at a phase detector. The electrical length difference corresponds to the wavelength of a 44 MHz signal. As a result, the phase detector will output zero voltage when the CT laser is directly on the desired frequency, and will diverge with opposite voltages on either side of that resonance. The VCO voltage provides fine tuning of the relative frequency difference between the lasers which allows the detuning of the CT laser to be adjusted.

2.3.3 Rydberg state excitation system

Transitions from the $5p_{3/2}, F = 2$ state to high n Rydberg states have wavelengths of approximately 480 nm. These wavelengths can be produced by frequency doubling the output of a 960 nm titanium sapphire (Ti:Saph) laser (Coherent, MBR-110). The Ti:Saph laser is pumped by a frequency doubled Nd:Vanadate laser (Verdi, V-10) which in turn is pumped by a diode laser.

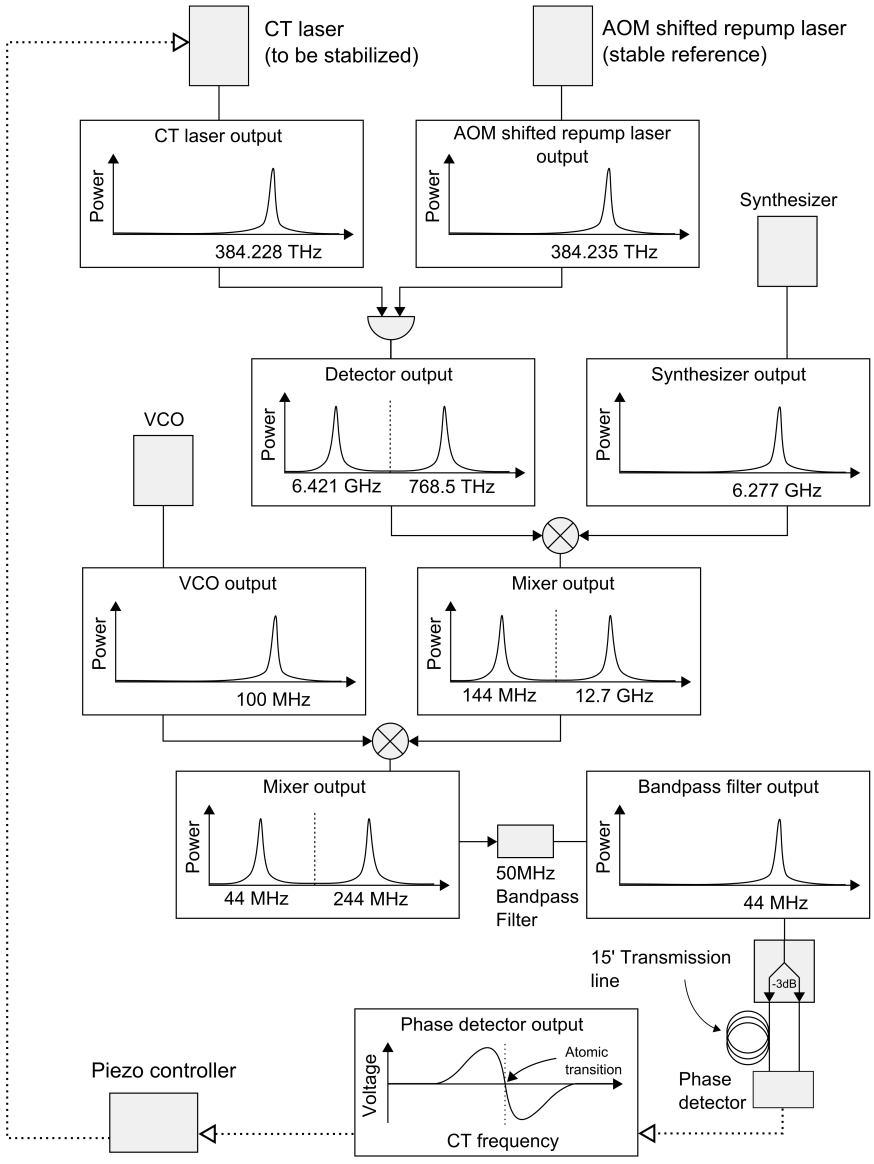

Figure 2.8: Derivation of the beat note signal. The 6.421 GHz beat frequency is first detected by a high bandwidth metal-semiconductor device. The signal is mixed with the output of a 6.277 GHz source followed by a tuneable 100 MHz VCO. The signal is then filtered and split between two different lengths of transmission line. A phase detector generates a signal from the two components which can be used in a feedback loop to stabilize the frequency of the CT laser.

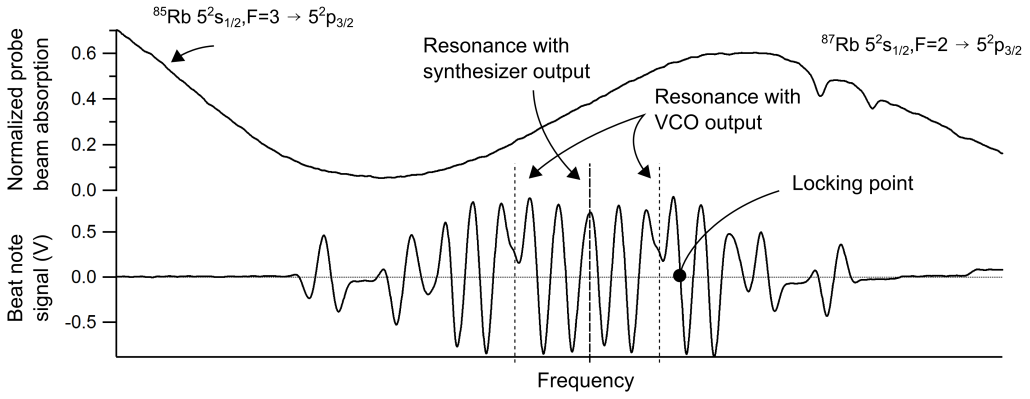

Figure 2.9: The SAS signal and output of the beat note system as a function of CT laser frequency. Symmetry points in the spectrum occur when the beat note frequency is resonant with the 6.277 GHz synthesizer signal, or when the downconverted signal is resonant with the 100 MHz VCO signal. The phase detector generates a signal which has opposite sign depending on whether the downconverted signal is above or below resonance with the 44 MHz transmission line interferometer.

The Ti:Saph wavelength is locked to the length of a cavity within the laser unit. This cavity is fabricated using low thermal expansion coefficient material, however it is still necessary to stabilize the length of this cavity relative to an external reference.

A stabilized transfer cavity acts as the external reference, as described in [8]. This transfer cavity is in turn stabilized relative to a diode laser which is injection locked by the repump laser (see Fig.2.10).

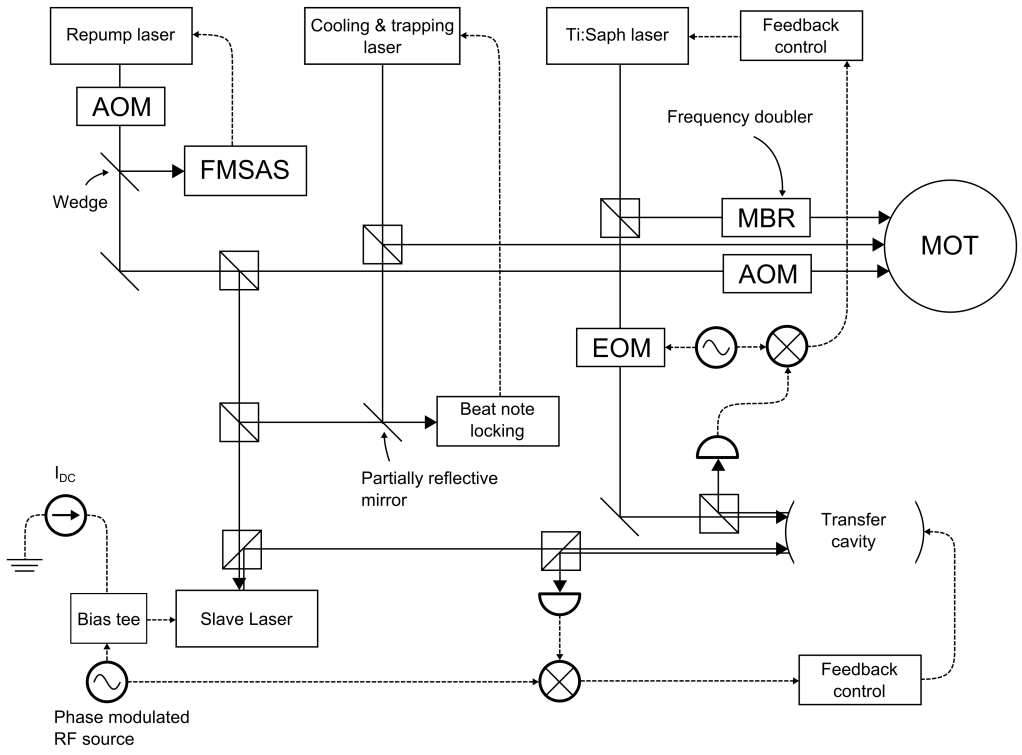

Figure 2.10: An overview of the laser stabilization system. The repump laser is used as a stable reference for the CT laser through a beat note system. The Ti:Saph laser is locked to a stabilized external transfer cavity. The transfer cavity is stabilized indirectly to the repump laser through an injection locked diode laser [8].

2.4 Imaging and population

For the sake of future experiments, an imaging system able to provide an estimate of the population of trapped atoms was calibrated. The 780 nm flouresence of the trapped atoms is imaged by a CCD camera positioned such that the cloud can be seen through a ø1/4" hole in the bottom field plate (Fig.2.11). The camera signal is digitized by a frame grabber and the intensity of the image is integrated. The numerical result is displayed, and can be correlated with the population of the MOT - provided no pixels in the image are saturated.

The correspondence between the image integration value and MOT population can be made by observing a 780 nm source with the camera and a photodiode from the same distance. The photodiode detects power, and can be used to determine the number of atoms required to produce such a signal. The photodiode is then swapped for the CCD camera to determine the corresponding integrated signal.

Using this system, the population was estimated to be on the order of 5×10^6 atoms early in the experiments. The beam alignment, beam balance, electric and magnetic fields have been optimized since those measurements giving a higher population.

2.5 Selective field ionization

The occupancy of individual Rydberg states is detected by ionizing the atoms and recording the output of a micro-channel plate (MCP) detector in a method called selective field ionization (SFI)[14]. The electric field which ionizes the atoms is ramped over the course of several microseconds and is applied across two field plates which are separated by 3.556 cm (Fig.2.11). The top field plate is grounded, and the positive ramping voltage is applied to the bottom field plate. The electric field forces the positive ions through a ø1/4" hole in the center of the top field plate and towards the micro-channel plate (MCP) detector. The front MCP is connected to a -1.5 kV source while the back MCP is held only slightly negative with respect to ground. The ions strike the front MCP and produce secondary electrons which are then drawn towards the back MCP, causing an electron avalanche. The amplified signal is detected by the anode, which is positioned behind the back MCP. This signal is amplified once again before being processed by a gated integrator and boxcar averager system which is synchronized with the SFI voltage pulse.

The ramping electric field ionizes atoms at different times depending on their energy. The ionization energy scales as $1/n^{*2}$ where n^* is the principle quantum number modified by the quantum defect [2]. The $49s_{1/2}$ and $48s_{1/2}$ states ionize at fields of 72.6 V/cm and 79.3 V/cm respectively. The gated integrators can be calibrated to sample over a period during which the signal for a particular energy state is generated. The signals for the two Rydberg

states involved in the transition of interest can be recorded and averaged for many shots.

2.6 Microwave coupling

This experiment requires us to apply dressing microwaves to atoms, and observe the effect of these microwaves on a transition between Rydberg states. A probe microwave field is applied to the atoms in the initial Rydberg state, and on resonance atoms are driven through a 2 photon $ns_{1/2} \rightarrow (n \pm 1)s_{1/2}$ transition to the final Rydberg state. Using a two photon transition ensures that the spectral line is not broadened by stray magnetic fields, since selection rules for a linearly polarized microwave field ensure that $\Delta m_j = 0$. For this apparatus, the best configuration for coupling the microwaves into the cavity involved coupling both the probe and dressing microwaves into the same rectangular horn using a 20 dB hybrid coupler (see Fig.2.12). The microwave horn faces the back of a dielectric mirror and $1/4\,\lambda$ wave plate which are used to reflect the CT light back into the vacuum chamber. These *retro-reflection* optics and their holder are sufficiently transparent to the microwave frequencies used. This configuration should minimize dressing microwave reflections, and prevent the formation of standing waves. This system is necessary to eliminate inhomogeneities in the dressing power which would cause spectral line broadening. The extent to which this helped is not clear. The coupler and rectangular horn can be rotated along the propagation

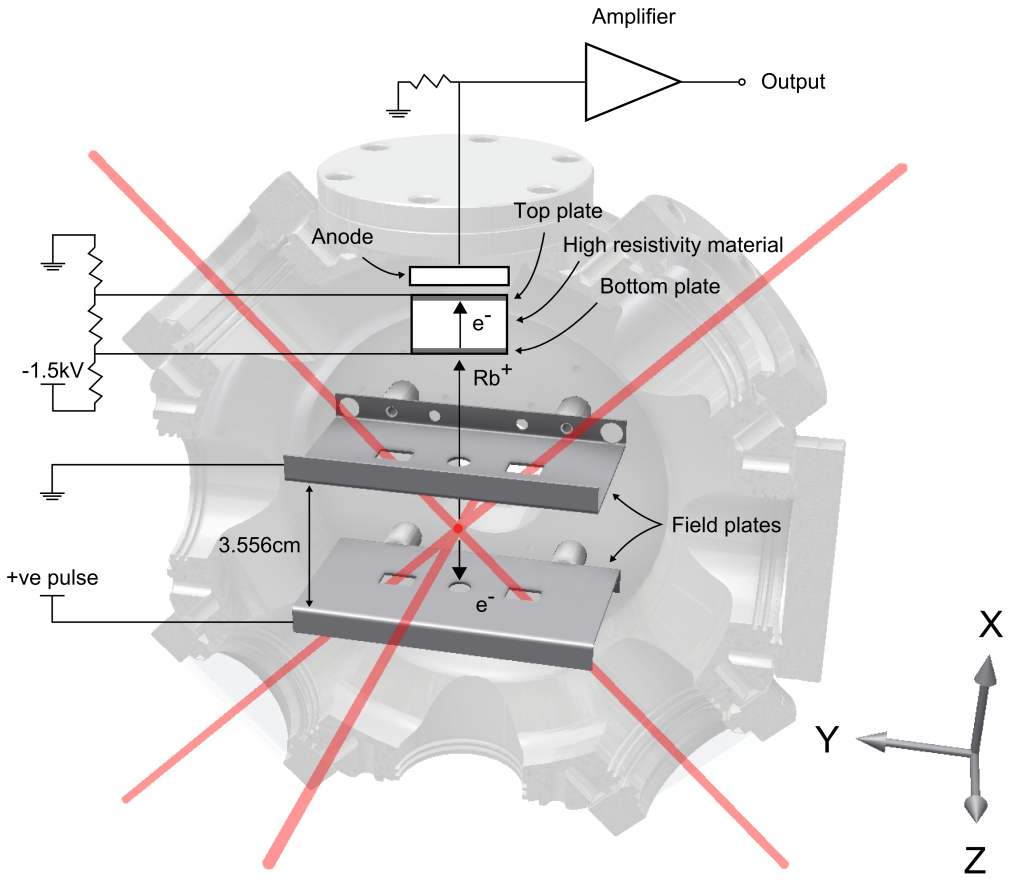

Figure 2.11: Schematic of the SFI system. The Rb ions strike the front micro-channel plate and cause an avalanche of secondary electrons which travel towards the back microchannel plate. The resulting signal is detected at the anode and is amplified.

axis, which is useful for investigating microwave polarization effects.

2.7 Experiment sequence

The experiment is repeated at a frequency of 10 Hz, and generally each probe frequency is sampled 20 times before moving to the next frequency in the spectrum. A shot of the experiment begins once a sufficient population of atoms is trapped (Fig.2.13). The AHC coils are shut off to reduce Zeeman splitting during the rest of the shot, however due to eddy currents this can take up to 20 ms [1]. The dressing and probe microwaves are left on while building MOT population and while waiting for AHC eddy currents to dissipate. Keeping the synthesizers on as long as possible allows the output power to stabilize. The dressing microwaves remain on shortly after the 36 μs probe pulse to ensure the dressing is steady over that 36 μs. During SFI, both the probe and dressing microwaves are turned off to avoid inducing adiabatic passage while the electric field is ramped. Once SFI is complete, the AHC's and microwaves are turned back on and the MOT population accumulates for the next shot. The experiment is synchronized with the 60 Hz line voltage using a delay generator.

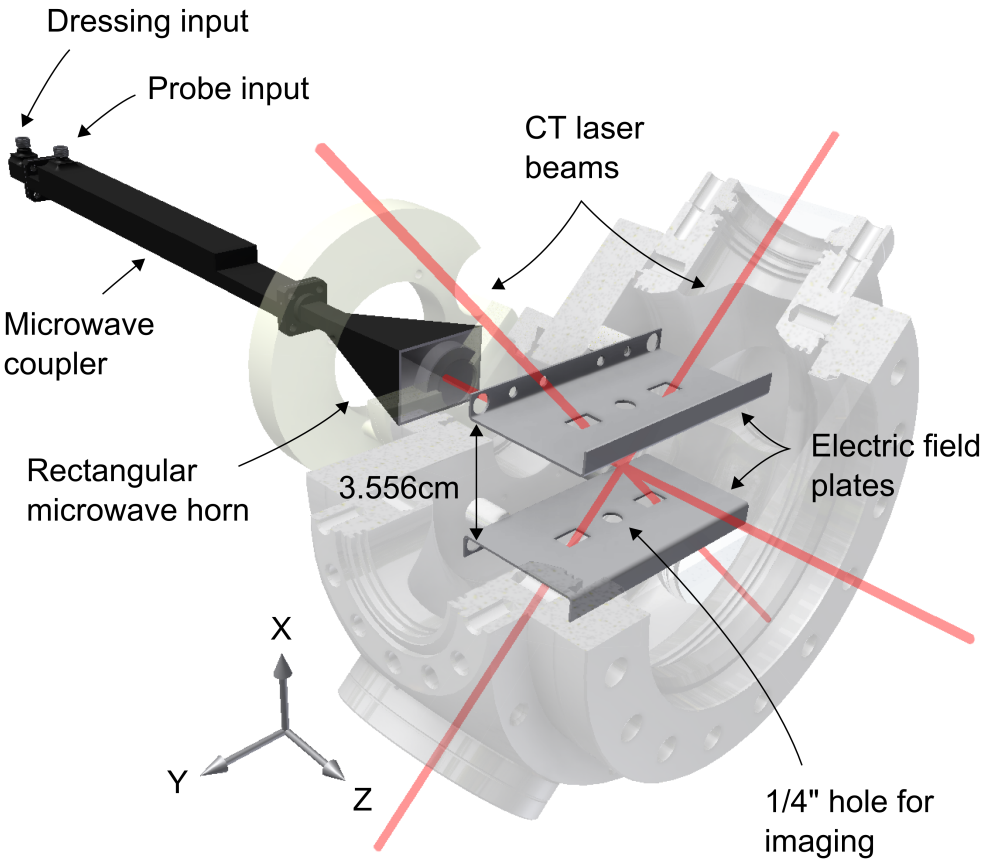

Figure 2.12: The orientation of the microwave horn relative to the retro-reflecting mirror, and vacuum chamber. The rectangular horn can be rotated on its axis to investigate effects of microwave polarization.

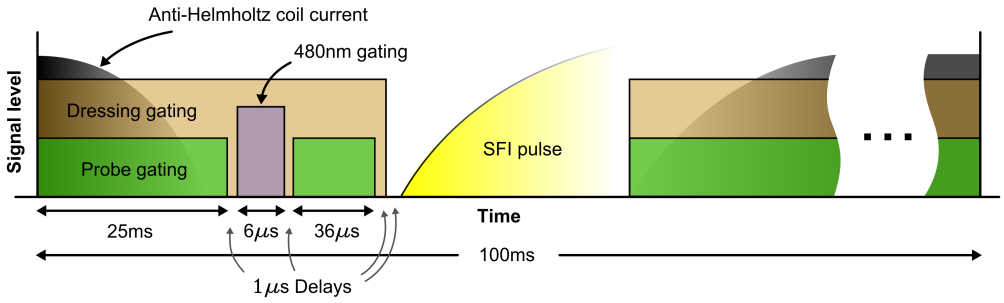

Figure 2.13: The experiment sequence. The experiment is synchronized with the line voltage to ensure that the effects of the line voltage are the same for each shot.

Chapter 3

Nulling experiment

3.1 Calculations

Floquet theory can be used to find the eigenvalues of the semi-classical combined atom/microwave field system [13]. The eigenvalues of this system are called *quasi-energies*, and the eigenstates are labeled by the *photon number* which indicates the number of photons in the microwave field. Since the microwave field is treated semi-classically, the photon number can take any value, resulting in an infinite basis set. For a sinusoidally oscillating field, only states differing in photon number by 1 are coupled (as discussed in section 3.1.1). As a result, a reduced basis which includes only states with a small range of photon numbers is needed for accurate results. In the following sections, the Floquet method is used to calculate energy levels in the presence of a microwave field. These calculations are then compared with

experimental results.

3.1.1 Dressing field equations

In the presence of a static electric field and oscillating electric field, the Schrödinger equation takes the form:

$$i\hbar\frac{\partial}{\partial t}F(t) = H(t)F(t), \tag{3.1}$$

where the *classical Hamiltonian* $H(t)$ of the atom is periodic in time, with periodicity ω. Along with the dc electric field necessary for this experiment, the classical Hamiltonian is

$$H(t) = H_o - \vec{\mu}\cdot(\vec{F_{dc}} + \vec{F_{ac}}\cos\omega t). \tag{3.2}$$

Here μ is the dipole moment operator and H_o is the zero field Hamiltonian of the atom. Floquet theory [13] states that the solution to such a differential equation can be written as

$$F(t) = \Phi(t)e^{-iQt}, \tag{3.3}$$

where Φ is a matrix of periodic functions and Q is a diagonal matrix of constants. This result can be used to write a more intuitive form of the Hamiltonian. To do this, the Φ matrix is Fourier transformed and the matrix

elements of the solution written as

$$F_{\alpha\beta}(t) = \Sigma_n F^n_{\alpha\beta} e^{in\omega t} e^{-iq\beta t}. \tag{3.4}$$

Likewise, the classical Hamiltonian is Fourier transformed:

$$H_{\alpha\beta}(t) = \Sigma_n H^n_{\alpha\beta} e^{in\omega t}. \tag{3.5}$$

Using this transformation, the classical Hamiltonian given by Eq.3.2 can be decomposed into a time independent component and a periodic component:

$$H^0_{\alpha\beta} = H_{o,\alpha\beta} - \vec{\mu_{\alpha\beta}} \cdot \vec{F_{dc}} \tag{3.6}$$

$$H^1_{\alpha\beta} = \frac{-\vec{\mu_{\alpha\beta}}}{2} \cdot \vec{F_{ac}}. \tag{3.7}$$

These terms can be substituted into the original Schrödinger equation to give the *Floquet Hamiltonian*:

$$\langle \alpha n | H_F | \beta m \rangle = \langle \alpha | H^{n-m} | \beta \rangle + n\omega \delta_{(\alpha-\beta)} \delta_{(n-m)}, \tag{3.8}$$

where n and m represent the number of photons, or *photon number* of the initial and final states of the combined atom/microwave field system. In this way, the time dependent Hamiltonian can be rewritten as a time independent, but infinite Floquet Hamiltonian (Fig.3.1).

The process of determining matrix elements for the Floquet Hamiltonian

involves first calculating the dipole moment matrix. The elements of the Floquet Hamiltonian are composed of dipole moment matrix elements with coefficients relating to the ac or dc field strength, depending on the difference between the photon numbers of the states. To determine the transition dipole moment between two states, the wavefunctions and dipole operator can be seperated into angular and radial components:

$$\mu_{z,i,f} = \langle \psi_{nlm,i}(r,\theta,\phi)|ez|\psi_{n'l'm',f}(r,\theta,\phi)\rangle \tag{3.9}$$

$$= e\langle \Theta^{m}_{l,i}(\theta,\phi)|\cos\theta|\Theta^{m'}_{l',f}(\theta,\phi)\rangle\langle R_{nl,i}(r)|r|R_{n'l',f}(r)\rangle. \tag{3.10}$$

The inner product of $\cos\theta$ can be found algebraically for spherical harmonic states [17]. The radial part of the dipole moment matrix is found using the Numerov technique [17].

Although it is practical to directly diagonalize the Floquet Hamiltonian in a finite basis set and obtain accurate results for this work (Sec.3.1.2), we may also use perturbation theory. Perturbation theory gives physical insight and allows us to quickly estimate suitable experimental parameters.

If the atom *in the presence of a static electric field* is the unperturbed system, then perturbation theory can give insight into the effect of deviations around that static electric field (given by ΔF_{dc}), as well as effects resulting from the ac field (F_{ac}). The perturbing Floquet Hamiltonian is written as:

	|1,n=1>	|2,n=1>	|3,n=1>	|1,n=0>	|2,n=0>	|3,n=0>	|1,n=1>	|2,n=1>	|3,n=1>
|1,n=-1>	$-\omega$	$-\mu_{1,2} \cdot F_{dc}$	$-\mu_{1,3} \cdot F_{dc}$	0	$\frac{-\mu_{1,2}}{2} \cdot F_{ac}$	$\frac{-\mu_{1,3}}{2} \cdot F_{ac}$	0	0	0
|2,n=-1>	$-\mu_{2,1} \cdot F_{dc}$	$-\omega$	$-\mu_{2,3} \cdot F_{dc}$	$\frac{-\mu_{2,1} \cdot F_{ac}}{2}$	0	$\frac{-\mu_{2,3} \cdot F_{ac}}{2}$	0	0	0
|3,n=-1>	$-\mu_{3,1} \cdot F_{dc}$	$-\mu_{3,2} \cdot F_{dc}$	$-\omega$	$\frac{-\mu_{3,1} \cdot F_{ac}}{2}$	$\frac{-\mu_{3,2} \cdot F_{ac}}{2}$	0	0	0	0
|1,n=0>	0	$\frac{-\mu_{1,2}}{2} \cdot F_{ac}$	$\frac{-\mu_{1,3}}{2} \cdot F_{ac}$	0	$-\mu_{1,2} \cdot F_{dc}$	$-\mu_{1,3} \cdot F_{dc}$	0	$\frac{-\mu_{1,2}}{2} \cdot F_{ac}$	$\frac{-\mu_{1,3}}{2} \cdot F_{ac}$
|2,n=0>	$\frac{-\mu_{2,1}}{2} \cdot F_{ac}$	0	$\frac{-\mu_{2,3}}{2} \cdot F_{ac}$	$-\mu_{2,1} \cdot F_{dc}$	0	$-\mu_{2,3} \cdot F_{dc}$	$\frac{-\mu_{2,1}}{2} \cdot F_{ac}$	0	$\frac{-\mu_{2,3}}{2} \cdot F_{ac}$
|3,n=0>	$\frac{-\mu_{3,1}}{2} \cdot F_{ac}$	$\frac{-\mu_{3,2}}{2} \cdot F_{ac}$	0	$-\mu_{3,1} \cdot F_{dc}$	$-\mu_{3,2} \cdot F_{dc}$	0	$\frac{-\mu_{3,1}}{2} \cdot F_{ac}$	$\frac{-\mu_{3,2}}{2} \cdot F_{ac}$	0
|1,n=1>	0	0	0	0	$\frac{-\mu_{1,2}}{2} \cdot F_{ac}$	$\frac{-\mu_{1,3}}{2} \cdot F_{ac}$	ω	$-\mu_{1,2} \cdot F_{dc}$	$-\mu_{1,3} \cdot F_{dc}$
|2,n=1>	0	0	0	$\frac{-\mu_{2,1}}{2} \cdot F_{ac}$	0	$\frac{-\mu_{2,3}}{2} \cdot F_{ac}$	$-\mu_{2,1} \cdot F_{dc}$	ω	$-\mu_{2,3} \cdot F_{dc}$
|3,n=1>	0	0	0	$\frac{-\mu_{3,1}}{2} \cdot F_{ac}$	$\frac{-\mu_{3,2}}{2} \cdot F_{ac}$	0	$-\mu_{3,1} \cdot F_{dc}$	$-\mu_{3,2} \cdot F_{dc}$	ω

Figure 3.1: A subset of the Floquet Hamiltonian. The atomic states are numbered, and n is the photon number of the atom/field combined system. The ac field couples states that have different photon numbers. The dark grey sub-matrices are the time independent components of the classical Hamiltonian and the lighter grey elements are the components of the classical Hamiltonian which are periodic. This pattern is repeated for an infinite number of photon number states.

$$\langle \alpha n | V | \beta m \rangle = \langle \alpha n | H_F - H_{F,o} | \beta m \rangle \tag{3.11}$$

$$= -\vec{\mu_{\alpha\beta}} \cdot \Delta F_{dc} \delta_{(n-m)} - \vec{\mu_{\alpha\beta}} \cdot F_{ac} \delta_{(|n-m|-1)}, \tag{3.12}$$

where H_F is the Floquet Hamiltonian which includes the ac field, dc field, and deviations from that dc field. $H_{F,o}$ is the Floquet Hamiltonian for the unperturbed system, which only includes the dc electric field.

In this experiment we are only interested in the leading order effect for both the F_{ac} and ΔF_{dc}, so we only require the first three terms of the perturbation theory expansion [7]:

$$E_n^{(1)} = V_{nn}, \tag{3.13}$$

$$E_n^{(2)} = \sum_k{}' \frac{|V_{kn}|^2}{\hbar(E_n^{(0)} - E_k^{(0)})}, \tag{3.14}$$

$$E_n^{(3)} = \sum_m{}' \sum_k{}' \frac{V_{nm}V_{mk}V_{kn}}{\hbar^2(E_n^{(0)} - E_m^{(0)})(E_n^{(0)} - E_k^{(0)})} - V_{nn} \sum_m{}' \frac{|V_{mn}|^2}{\hbar^2(E_n^{(0)} - E_m^{(0)})^2}. \tag{3.15}$$

Here, primed summation implies the index n is excluded. The first order energy perturbation term for the state αn is

$$E_{\alpha n}^{(1)} = -\mu_\alpha \Delta F_{dc}, \tag{3.16}$$

where μ_α is the static electric field induced electric dipole moment (to be referred to as the *dipole moment*) of state αn. The Greek symbols label the atomic state while the Latin symbols signify the photon number. The second order term is

$$\begin{aligned} E_{\alpha n}^{(2)} =& \sum_{\beta m}{}' \frac{|V_{\alpha n,\beta m}|^2}{\hbar(E_n^{(0)} - E_m^{(0)} + (n-m)\omega)} && (3.17) \\ =& \sum_{\beta m}^{m=n,\beta\neq\alpha} \frac{|-\vec{\mu_{\alpha\beta}} \cdot \Delta\vec{F}_{dc}|^2}{\hbar(E_\alpha^{(0)} - E_\beta^{(0)} + (n-m)\omega)} \\ &+ \sum_{\beta m}^{m\neq n} \frac{|-\vec{\mu_{\alpha\beta}} \cdot \vec{F_{ac}}|^2}{\hbar(E_\alpha^{(0)} - E_\beta^{(0)} + (n-m)\omega)} && (3.18) \\ =& \alpha_{\alpha n}(\omega) F_{ac}^2, && (3.19) \end{aligned}$$

where the second order term in ΔF_{dc} has been discarded. $\alpha_{\alpha n}(\omega)$ is proportional to the ac polarizability of state αn. The third order term is derived similarly, and includes all permutations of three field dependances, each of which could be ΔF_{dc} or F_{ac}. The third order pertubation to energy, after discarding terms which are not lowest order in either of the perturbations, is

$$E^{(3)}_{\alpha n} = \beta_{\alpha n}(\omega)\Delta F_{dc}F^2_{ac}. \tag{3.20}$$

The factor $\beta_{\alpha n}(\omega)F^2_{ac}$ can be interpreted as an electric dipole moment which can be tuned using the ac field strength and frequency. The total energy of state αn is

$$E_{\alpha n} = E_{o,\alpha n} - \mu_\alpha \Delta F_{dc} + \alpha_{\alpha n}(\omega)F^2_{ac} + \beta_{\alpha n}(\omega)\Delta F_{dc}F^2_{ac}. \tag{3.21}$$

The relative energy shift between two states is given by

$$\Delta E \approx \Delta E_o - (\mu_\alpha - \mu_\beta)\Delta F_{dc} + (\alpha_\alpha(\omega) - \alpha_\beta(\omega))F^2_{ac} + (\beta_\alpha(\omega) - \beta_\beta(\omega))\Delta F_{dc}F^2_{ac} \tag{3.22}$$

Where the photon number designation has been dropped, as it is the same for both states. In an electric field, different states will have different dipole moments such that the second term in Eq. 3.22 is non-zero. As a result, the energy difference between the states changes with deviations from the static electric field (in the absence microwave fields). This sensitivity to the electric field deviations can be eliminated by counterbalancing the difference

between dipole moments with the difference between *ac field induced dipole moments*:

$$-(\mu_\alpha - \mu_\beta) + (\beta_\alpha(\omega) - \beta_\beta(\omega))F_{ac}^2 = 0. \tag{3.23}$$

It is useful to define $\Delta\mu = \mu_\alpha - \mu_\beta$, $\Delta\alpha(\omega) = \alpha_\alpha(\omega) - \alpha_\beta(\omega)$, and $\Delta\beta(\omega) = \beta_\alpha(\omega) - \beta_\beta(\omega)$ such that Eq. 3.23 can be written as

$$-\Delta\mu + \Delta\beta(\omega)F_{ac}^2 = 0. \tag{3.24}$$

The dipole moment difference can be eliminated with any frequency where $\Delta\beta(\omega)$ is the same sign of $\Delta\mu$ (Fig. 3.2). Equation 3.24 can then be satisfied by applying the appropriate amount of ac power. This constraint does not uniquely determine the dressing frequency, so the remaining freedom is used to eliminate the difference between the ac polarizabilities of the two states. With matched ac polarizabilities, the energy difference between the states is less sensitive to spatial inhomogeneities in the dressing field power. These two conditions; $\Delta\beta$ having appropriate sign, and $\Delta\alpha$ being zero, is enough to narrow the dressing frequency to several possibilities. The choice between possible dressing frequencies can be made by weighing the convenience of producing power at the frequency and the importance of minimizing the amount of dressing power required (discussed further in section 3.2.2).

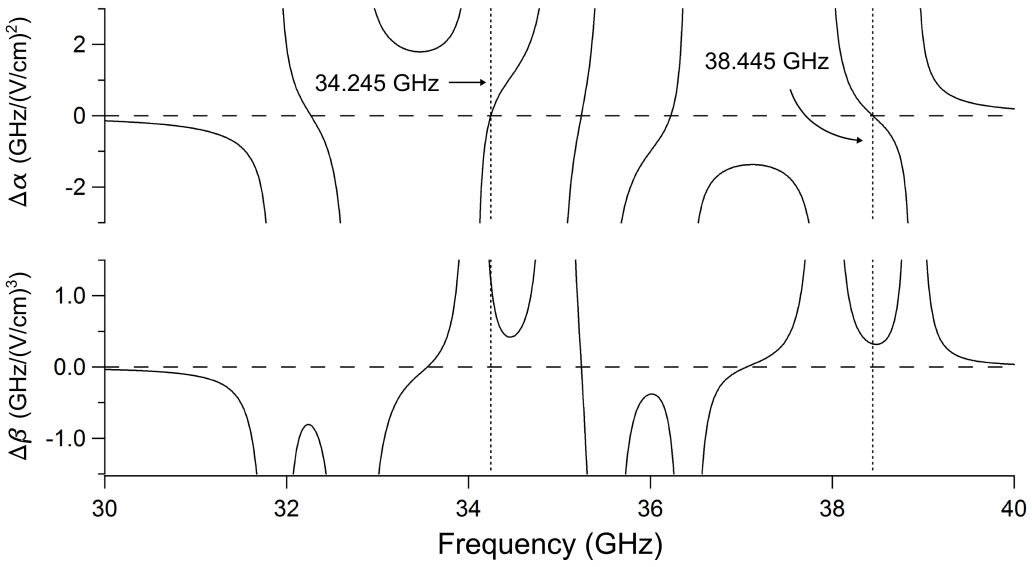

Figure 3.2: Difference between a) the ac polarizability coefficients and b) the third order perturbation term coefficients for $49s_{1/2}, m_j = 1/2$ and $48s_{1/2}, m_j = 1/2$ in the presence of a 1 V/cm electric field. The functions diverge near resonances with atomic transitions involving either of the states.

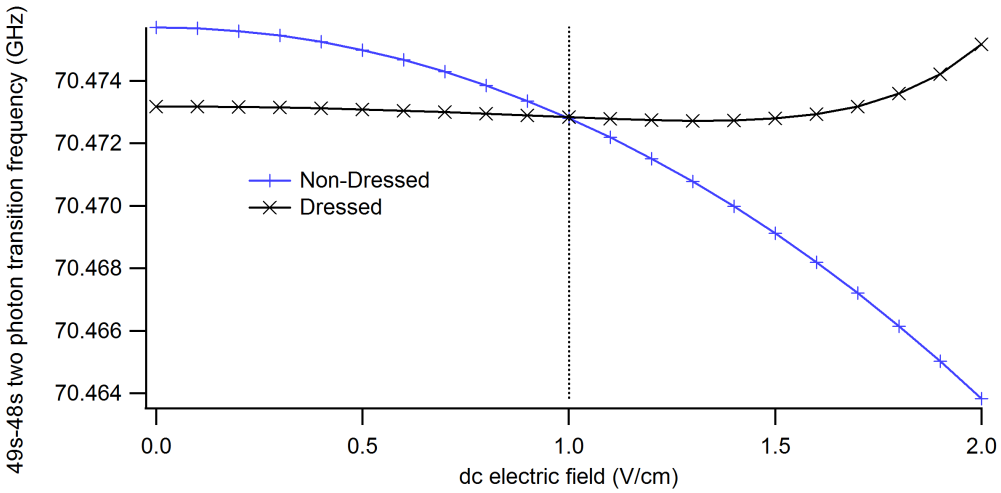

Figure 3.3: The Floquet calculation of the $49s_{1/2}, m_j = 1/2 \rightarrow 48s_{1/2}, m_j = 1/2$ transition frequency as a function of dc field a) without dressing, and b) in the presence of a dressing microwave field. The parameters of the microwave field were determined by the perturbation theory procedure and are set to 38.445 GHz and 0.1305 V/cm. Note that at 1 V/cm there is no ac Stark shift or first order dependence on the dc electric field.

3.1.2 Matrix diagonalization

To confirm that the perturbation theory approach of the previous section has provided correct dressing field parameters, we can generate dressed and non-dressed Stark maps by diagonalizing a reduced basis Floquet Hamiltonian (Fig.3.3 and Fig.3.4). If the ac polarizability difference is zero, then the energy difference should be independent of the dressing microwave power as long as the perturbation theory approximation remains valid. For stronger dressing fields, higher order terms in the perturbation expansion will begin to contribute and the energy difference will change.

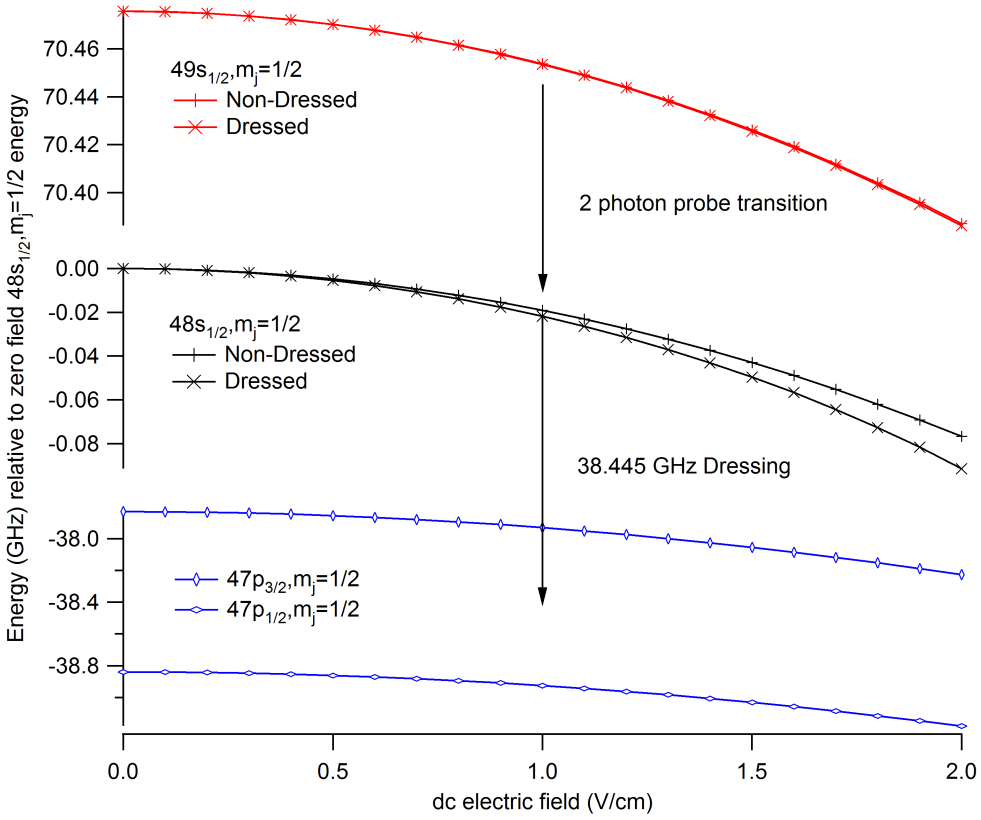

Figure 3.4: Stark shifted energy levels with and without microwave dressing. The dipole moment of $48s_{1/2}$ is modified due to coupling with the $47p$ states using a 38.445 GHz and 0.1305 V/cm microwave field.

3.2 Results

3.2.1 Low n experiments

The experiment was initially performed on the $36s_{1/2} \rightarrow 35s_{1/2}$ transition, since the Ti:Sapphire laser had operated reliably at the required wavelength in previous experiments. The electric field was set to 1 V/cm. Initial observations of the spectral line showed broadening which depended on the dressing microwave power. The effect was strong enough to completely suppress the spectral line with just a fraction of the dressing microwave power required for the nulling experiment. The cause of the broadening was found to be noise in the microwave dressing, which drives transitions from either of the Rydberg states (discussed in more detail in Chapt.4). In addition to reducing the lifetimes of Rydberg states and causing broadening, the atoms are also driven to undetected states. If the initial Rydberg state is being depleted, the relative population of final Rydberg state increases and consequently the noise floor increases. If the final Rydberg state is depleted, the relative population of the initial Rydberg state increases and consequently the amplitude of the spectral line is reduced.

The source of the noise was found to be the amplifying quadrupler used to produce microwaves at the dressing frequency. Several designs of waveguide filters have been investigated to reduce the microwave noise. Although performing the experiment with this transition was pursued, a transition with a more convenient dressing frequency was used to demonstrate the experimen-

tal result. Development of the microwave filters is discussed in Chapt.4.

3.2.2 High n experiments

The $49s_{1/2} \rightarrow 48s_{1/2}$ transition is at roughly 33 GHz, and requires a dressing frequency of either 34.245 GHz or 38.445 GHz for nulling, based on the considerations discussed in section 3.1.1. As these frequencies can be produced by our synthesizers, the amplifying quadrupler is not required and the noise it produces is avoided. For either of the dressing frequencies, the spectral line splits into a doublet which widens as the dressing power is increased. One hypothesis to explain this doublet is that the splitting is the result of slight ellipticity in the otherwise linear microwave dressing field. This ellipticity could arise from imperfections in the rectangular horn used to couple into free space, or reflections from surfaces in the vacuum chamber. For 38.445 GHz dressing, splitting would result because different magnetic sublevels of the $48s_{1/2}$ would couple to one another through a $47p_{1/2}$ or $47p_{3/2}$ magnetic sublevel. The 34.245 GHz dressing frequency would couple the $49s_{1/2}$ magnetic sublevels through a $49p_{1/2}$ or $49p_{3/2}$ magnetic sublevel. The transition dipole moment for the $s \rightarrow p$ transition is much stronger than the two photon $s \rightarrow s$ transition, which explains why even a small amount of ellipticity can cause a significant amount of splitting. As an example, one of the coupling terms with 38.445 GHz would connect $48s_{1/2}, m_J = -1/2$ to $47p_{1/2}, m_J = 1/2$ through a σ transition, and then to $48s_{1/2}, m_J = 1/2$ through a π transition.

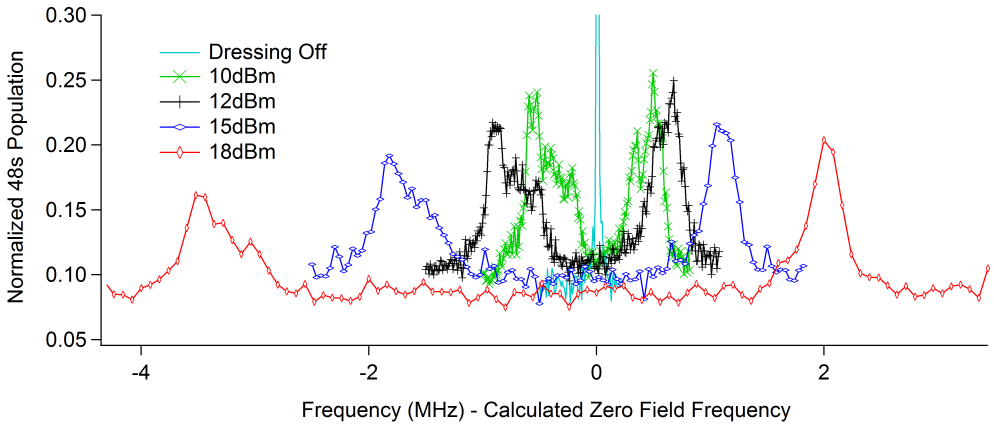

Figure 3.5: Splitting of the $49s_{1/2}, m_j = 1/2 \rightarrow 48s_{1/2}, m_j = 1/2$ two photon spectral line. This is caused by ellipticity in the dressing microwave field which allows coupling between the magnetic sublevels of the 48s state.

To verify that microwave ellipticity is the cause of the doublet, the ellipticity can be modified in several ways. To check whether reflections from within the vacuum chamber cause ellipticity, the line splitting can be observed as the microwave horn is rotated on the z axis. The result of this experiment was that the splitting between the lines *is* modified by rotating the horn, however a significant portion of the splitting is independent of rotation.

Another test that can be done is to modify the ellipticity of microwaves at the center of the vacuum chamber. To do this, a second microwave field can be applied which has an approximately orthogonal polarization, controllable phase and controllable amplitude. This can be done using a second microwave horn pointing in the -z,-y direction, a variable attenuator and a translation mount. One synthesizer produces the dressing signal, which is split and sent to the two horns. One arm of the circuit is attenuated and the horn

is moveable such that the relative phase between the dressing fields at the center of the vacuum chamber is adjustable. What we observe with this test is that the magnitude of the splitting oscillates with a period equal to half the dressing field wavelength. This is consistent with the idea that the splitting is caused by ellipticity, since the polarization would change from elliptical to linear and back to elliptical with a phase change of 180 degrees.

To reduce the ellipticity, it is necessary to counteract any effect of horn imperfections or reflections within the vacuum chamber by controlling the polarization. One way to do this is to couple two orthogonal microwave fields in an orthomode coupler with a controllable relative phase and amplitude. This would then couple into the vacuum chamber using a circular horn.

Even while the spectral lines split with microwave power, the nulling experiment can be performed on one of the doublet peaks. Figure 3.6 shows the results of this experiment to eliminate the dipole moment difference at 1 V/cm. The ac polarizability of the states is not matched for this dressing frequency, which causes the nulled spectral line to be shifted from the zero ac field frequency.

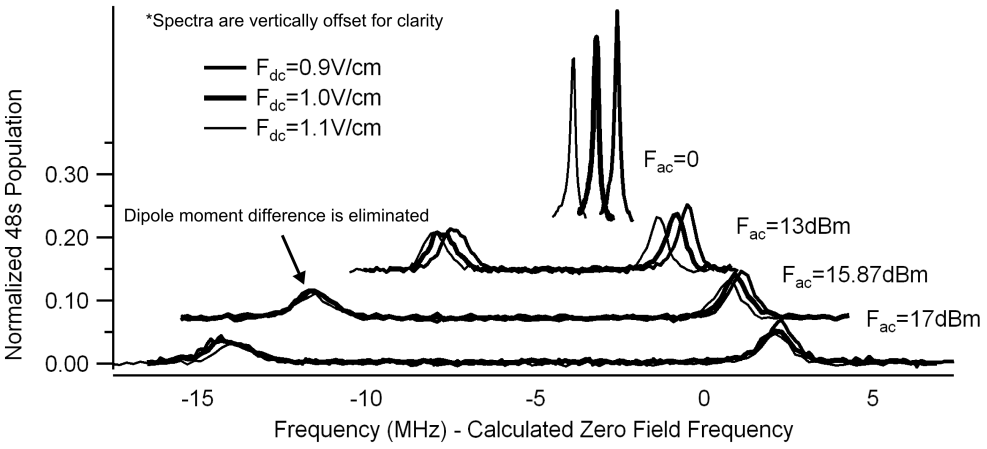

Figure 3.6: Demonstration of dipole moment difference nulling for the $49s_{1/2}, m_j = 1/2 \rightarrow 48s_{1/2}, m_j = 1/2$ transition. Each set of three overlapping plots denotes spectra taken with and without $\pm 0.1\,\mathrm{V/cm}$ deviations about the $1\,\mathrm{V/cm}$ static electric field for a constant dressing microwave power. The dressing microwave power is different for each set of three plots. The electric dipole moment difference is eliminated for one of the doublet peaks at a particular dressing power, as indicated by the constant spectral line frequency despite deviations about the static electric field.

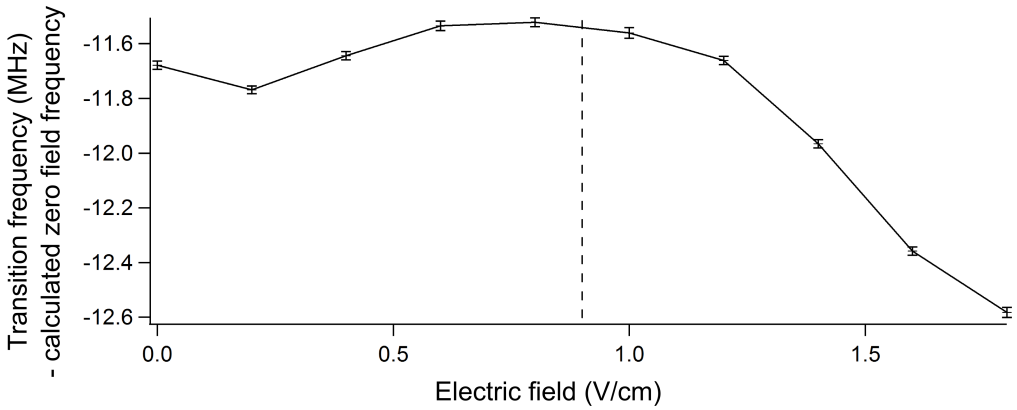

Figure 3.7: The dressed transition frequency as a function of dc electric field. At 1 V/cm the dipole moment difference between the two states (as indicated by the slope of the function) was nearly eliminated by applying a microwave dressing field of 38.525 GHz and 15.87 dBm. The dressing frequency and power used was found empirically, and therefore might not demonstrate the nulling result as precisely as possible.

Chapter 4

Microwave filtering

4.1 Identifying the noise source

Based on considerations discussed in previous chapters, a suitable dressing frequency for nulling the dipole moment difference between the $36s_{1/2}$ and $37s_{1/2}$ states is 98.34 GHz. To produce this frequency, the output of a 40 GHz frequency synthesizer is multiplied by an active quadrupler. The quadrupler has an internal amplifier and the output is also amplified to generate the necessary microwave power. Early experiments showed that rather than a pure ac Stark shift, the spectral line associated with the $36s_{1/2} \rightarrow 37s_{1/2}$ transition instead broadens as it is ac Stark shifted (see Fig.4.1). The cause of the dressing power dependant broadening was found to be noise at the input of the quadrupler which mixes with the deliberately applied input. We can verify this hypothesis by looking at how the spectral noise density of the

quadrupler output scales with the carrier power. The spectral noise density can be calculated from the line width, while the ac Stark shift can be used to determine the carrier power. The output noise power scaling can be derived by noting that any noise photon which enters the quadrupler will be mixed with input carrier photons. The dominant source of output noise results from the mixing of one input noise photon with three input carrier photons (Fig.4.2):

$$(OutputNoise) \propto (InputCarrier)^3 \cdot (InputNoise). \tag{4.1}$$

The dominant scaling of the output carrier power will come from mixing four input carrier photons:

$$(OutputCarrier) \propto (InputCarrier)^4. \tag{4.2}$$

The scaling of the output noise power relative to the output carrier power can be found by combining 4.1 and 4.2:

$$(OutputNoise) \propto (OutputCarrier)^{3/4} \cdot (InputNoise). \tag{4.3}$$

Experimental data supports this theory (see Fig.4.3), and shows that the observed spectral line width scaling is approximately $(OutputCarrierPower)^{3/4}$.

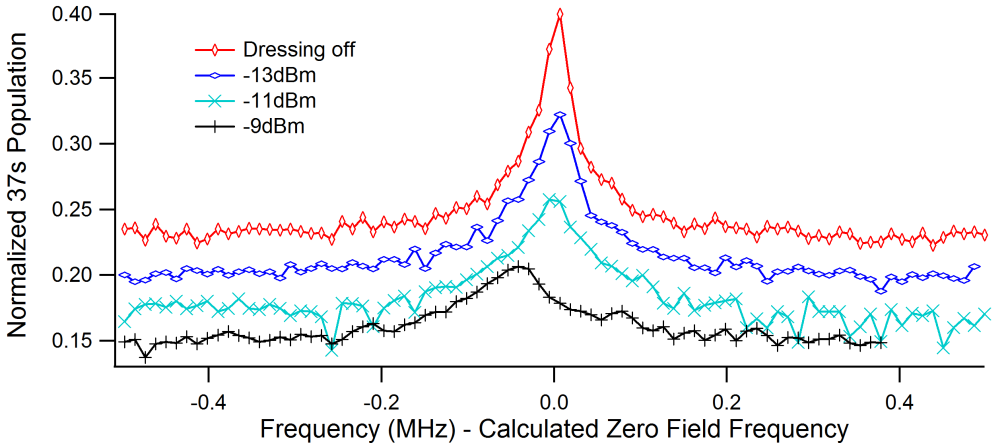

Figure 4.1: Unfiltered spectral lines for the $36s_{1/2} \rightarrow 37s_{1/2}$ transition in 0 V/cm and under the influence of a 94.226 GHz microwave field.

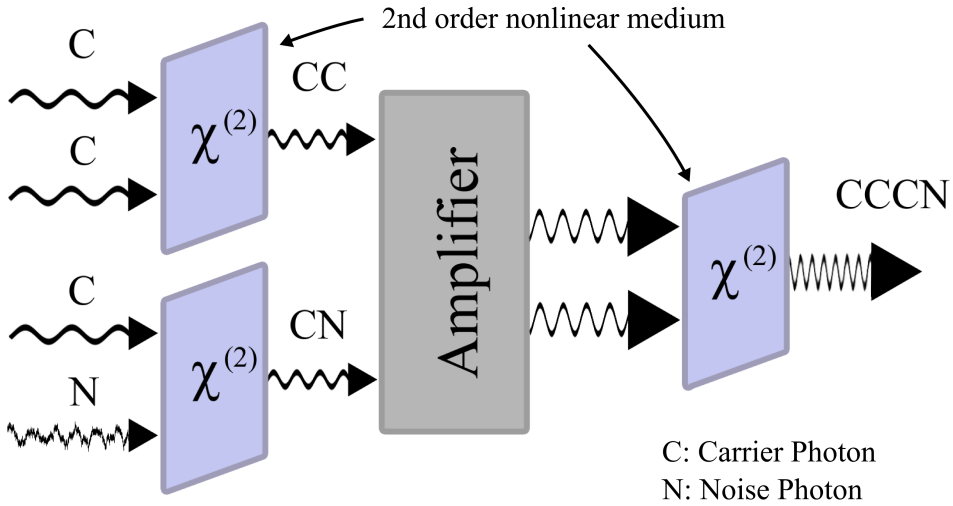

Figure 4.2: Mechanism by which noise is introduced to the carrier. Frequency multiplication occurs in crystals having a $\chi^{(2)}$ non-linearity.

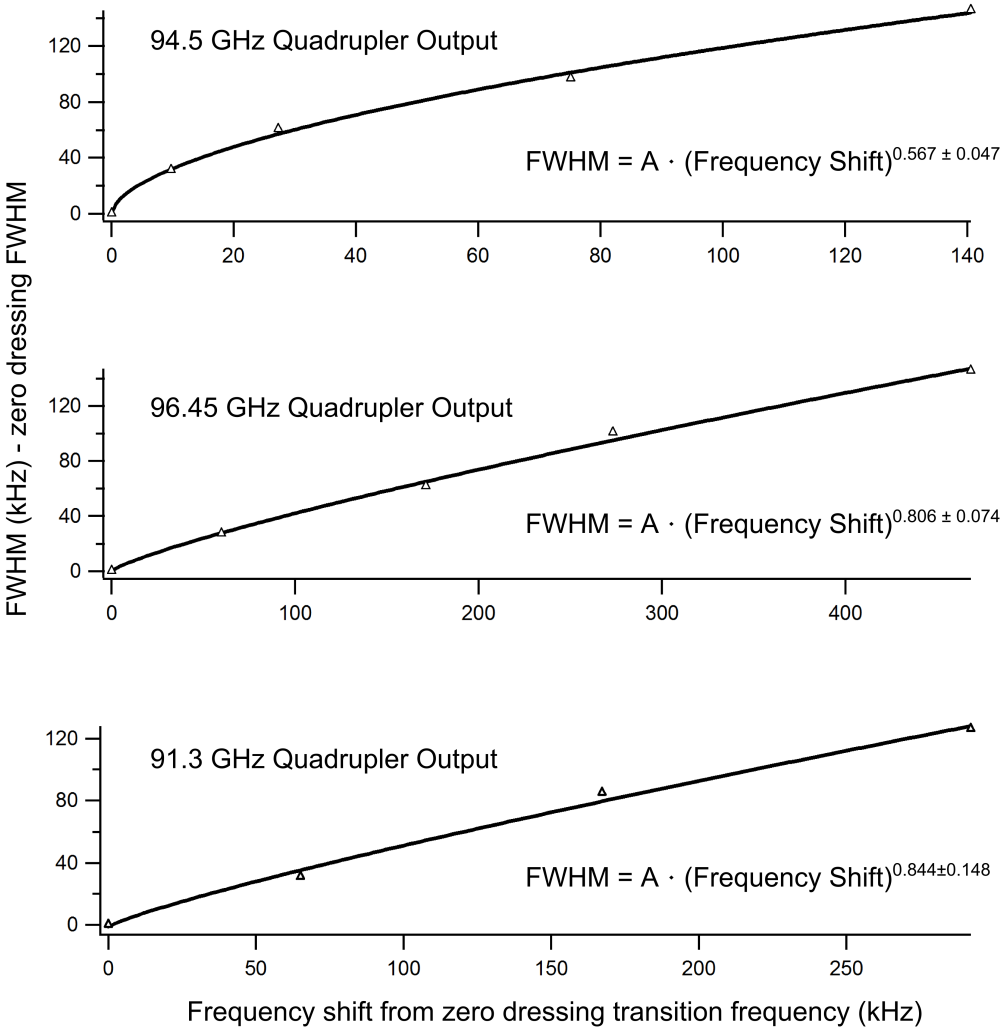

Figure 4.3: Scaling of the output noise power relative to the output carrier power for three different dressing frequencies.

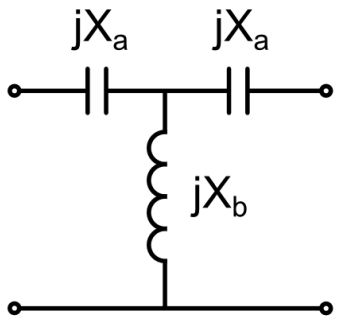

Figure 4.4: Lumped element equivalent circuit for waveguide post and iris discontinuities.

4.2 General filter designs

To reduce the spectral noise density of the dressing microwave field, the output of the quadrupler can be filtered. Commercial filters are not readily available for this frequency, which motivated us to design and fabricate our own. At 98.34 GHz the lowest losses would be achieved by implementing the filter in waveguide. The insertion loss method [9][11] can be used to design a lumped element circuit for the required filter (see Fig.4.5). This circuit can be implemented in waveguide using either inductive posts [16](Fig.4.7), or inductive irises (Fig.4.10) - both are discussed. Post and iris discontinuities have an equivalent circuit shown in Fig.4.4 where X_a is zero for ideal thin irises and non-zero for thick irises. The circuit parameter calculation assumes $X_a = 0$.

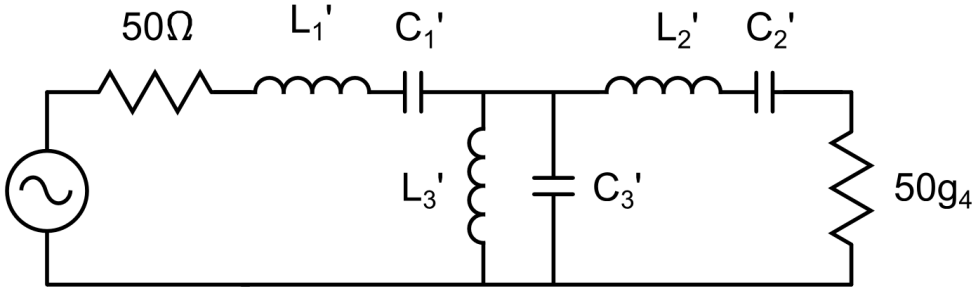

Figure 4.5: A lumped element circuit band-pass filter. The component values are determined by applying frequency and impedance transformations to low-pass prototype circuit elements. Band-pass fall off and complexity are considered when deciding the clas of filter and number of elements.

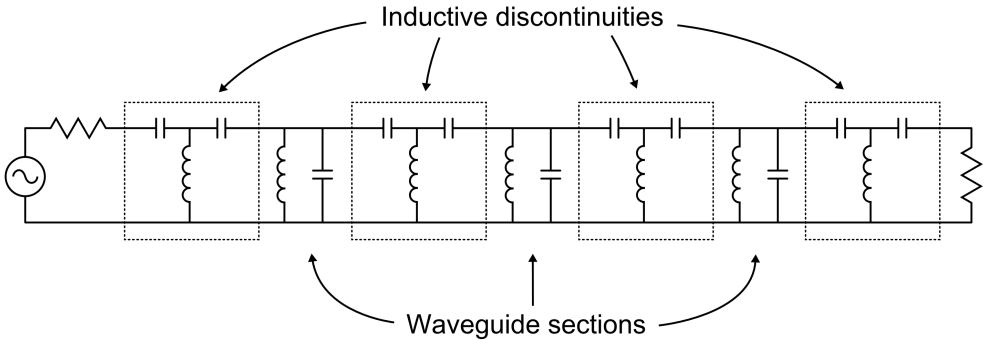

Figure 4.6: Band-pass filter circuit in a form which can be easily implemented using waveguide sections with inductive discontinuities.

4.2.1 Post filters

The waveguide post filter design (Fig.4.8) is the easiest to implement when starting with prefabricated sections of rectangular waveguide. For our purposes we used sections of brass WR10 rectangular waveguide which are appropriate for 90 GHz to 140 GHz. The manufacturing technique involves drilling holes through the waveguide and silver soldering tightly fitted posts in place. If a tuneable filter is required, then screws are installed between each pair of posts, penetrating one wall of the waveguide. Brass 000-120 screws are small enough for this purpose. The screw is threaded through a piece of brass which is silver soldered to the top of the waveguide. Adding this material allows the tuning screws to be threaded through more material making them fit tighter, and as a result making adjustment easier. The excess material is then removed either by a mill or slitting saw, and holes are drilled for the posts. The posts are silver soldered in place with low temperature solder, or alternatively they can be secured with silver bearing epoxy.

This method is effective for fabricating non-tuneable filters, however the extra steps involved in adding tuning screws, and also unreliable steps such as silver soldering flanges makes this method unappealing. A better method involves cutting square channels in opposing faces of brass blocks (Fig.4.9) such that when they are secured together, a section of waveguide is formed. The posts are held between semi-circle grooves cut into the opposing faces, and tuning screws are held between threaded semi-circle grooves. The two halves of the *split block post filter* are fitted with guide pins that allow reliable

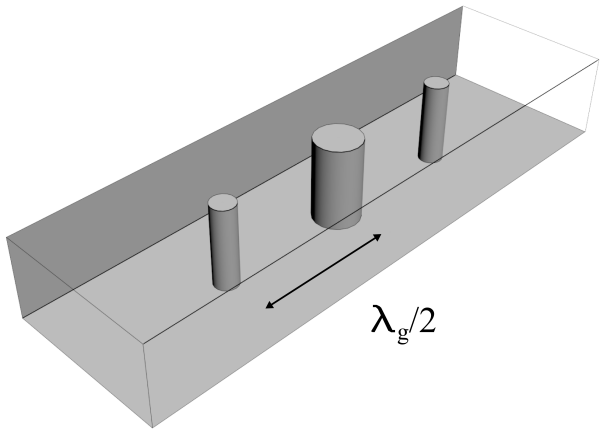

Figure 4.7: Schematic of a two element post filter. The tuning screw would be positioned above and inserting into each of the cavities formed between posts.

alignment during assembly. The channels which form the waveguide are milled into the brass blocks by a high RPM CNC, which also scribes tracks where the tuning screws and posts will be installed. The pieces are assembled and the scribed tracks serve to guide the appropriate drill bits for the post and screw holes. The tuning screw holes can then be tapped. The post holes are drilled slightly over size, and then tightened by sanding down both halves of the filter. Sanding down the halves has a small effect on the overall dimensions of the waveguide, but it is hoped that doing this increases the conductivity between the posts and the inner surfaces of the waveguide, and prevents the posts or tuning screws from moving.

Split block post filters are easier to build than the prefabricated waveguide filters, however the process is still time consuming since the two halves need to be sanded by hand to tighten the posts and tuning screws. A second type of

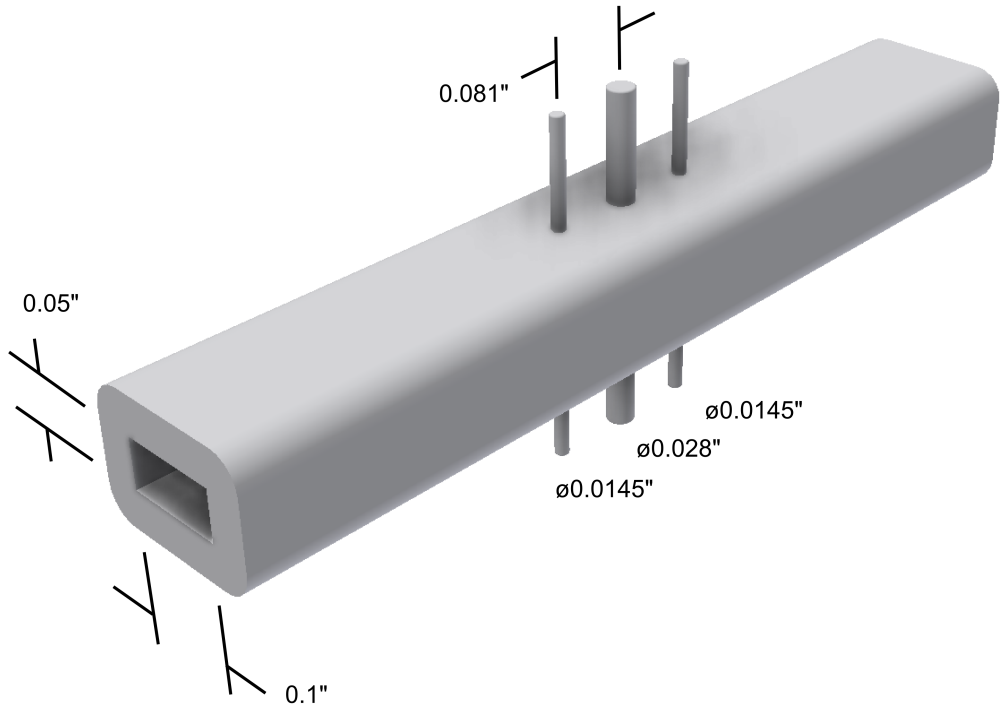

Figure 4.8: A two element waveguide post filter. The portions of the inductive posts protruding from the outer surface are remnants from the manufacturing procedure, and serve no purpose but to suggest the internal structure of the filter.

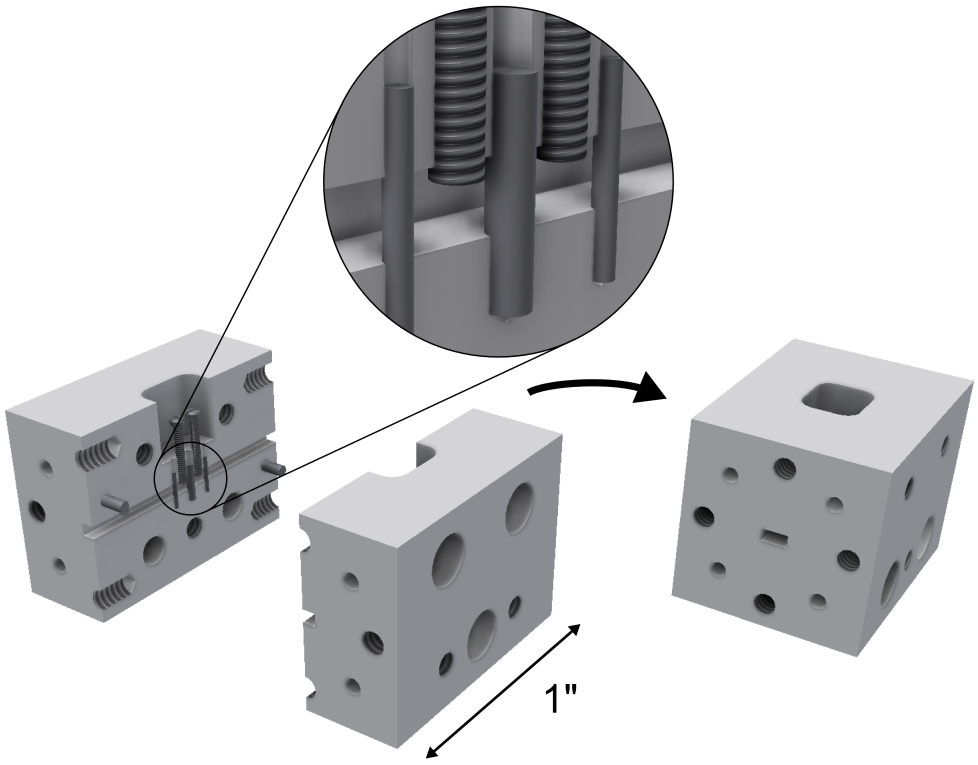

Figure 4.9: A two element split-block post filter. Guide pins ensure the two halves are properly aligned. The posts and screws are installed in semi-circle grooves that are machined by drilling into the assembled filter along scribed tracks. The fit can be tightened by sanding the mating faces.

split block filter was developed in parallel, which relies on iris discontinuities rather than post discontinuities. Iris filters have the advantage that posts do not need to be installed, which makes fabrication much faster.

4.2.2 Iris filters

The third design is based on an inductive iris implementation of the lumped element circuit (Fig.4.10). The calculation to find the iris dimensions assumes that the irises are infinitely thin. To ensure that the finite thickness does not alter the bandwidth of the filter significantly, the iris thickness needs to be kept to several percent of the resonator length [9]. An iris thickness of 0.005" was found to be the minimum thickness achieveable, since the iris fins would not reliably survive the milling process with any less support. When the blocks are assembled, the two fins form a rectangular iris which inductively couples the resonating elements of the filter (Fig.4.11). The concave corners in the filter must have a radius in some spots, however the results show that a radius of 1/64" results in negligible deviation from the calculated resonant frequency.

4.3 Results

Before developing the split block filter designs, we verified that filtering is effective at reducing the broadening of the microwave dressed spectral lines. This test was performed using a section of waveguide terminated at either

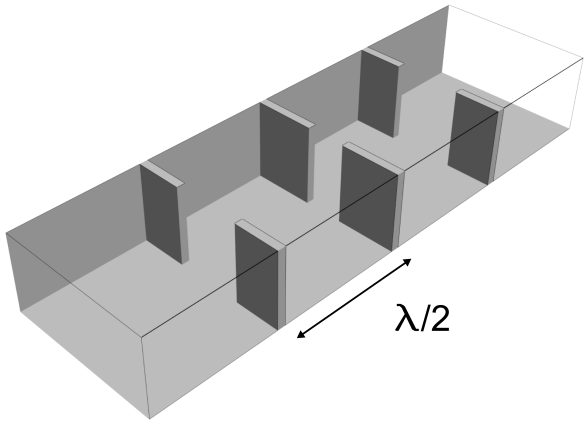

Figure 4.10: Schematic of a two element iris filter. The tuning screw would be positioned above and inserting into each of the cavities formed between irises.

end by circular irises. This enclosed segment formed a resonator that could be tuned by milling away waveguide material. Using this filter, a significant reduction in the amount of broadening was observed, as seen in Fig.4.13.

Next, using a two element tuneable block iris filter, the test was performed again. The amount of dressing that could be applied before the spectral line became indistinguishable was increased significantly. The fact that the baseline increased as the unfiltered dressing power was increased suggests that a transition from the ground state is being driven by white noise.

4.4 Filter conclusions

The three element block iris filter should have sufficient attenuation to limit broadening for the full amount of dressing power required to perform the

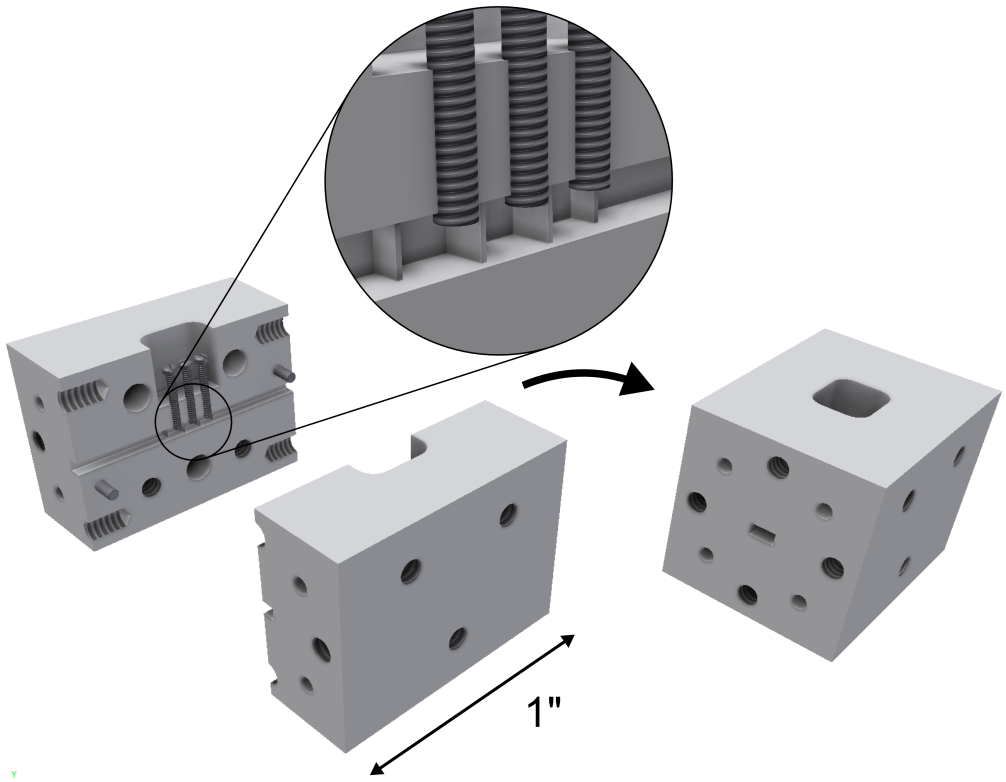

Figure 4.11: Assembly of the split-block iris filter. This design is more simple to build than post the split-block post filter since the posts do not need to be installed. The thickness of the fins that form the irises when assembled must be at least 0.005" thick to reliably survive the manufacturing process.

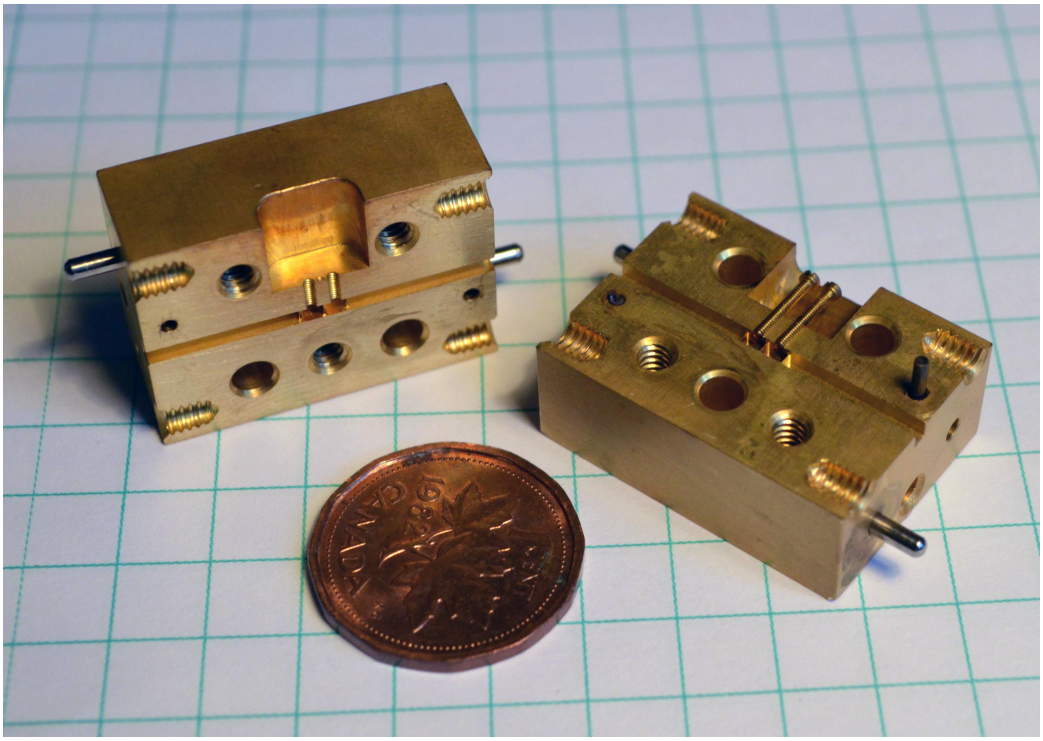

Figure 4.12: A tuneable spit-block iris filter with two resonating sections.

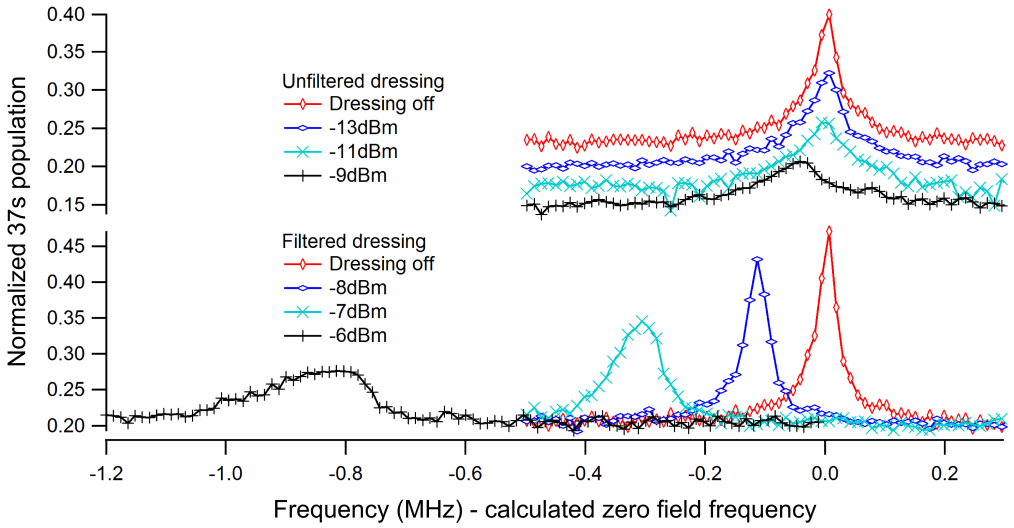

Figure 4.13: Spectral lines of the $36s_{1/2} \rightarrow 37s_{1/2}$ transition under the influence of a 94.226 GHz microwave field, filtered by a section of rectangular waveguide with circular iris end caps.

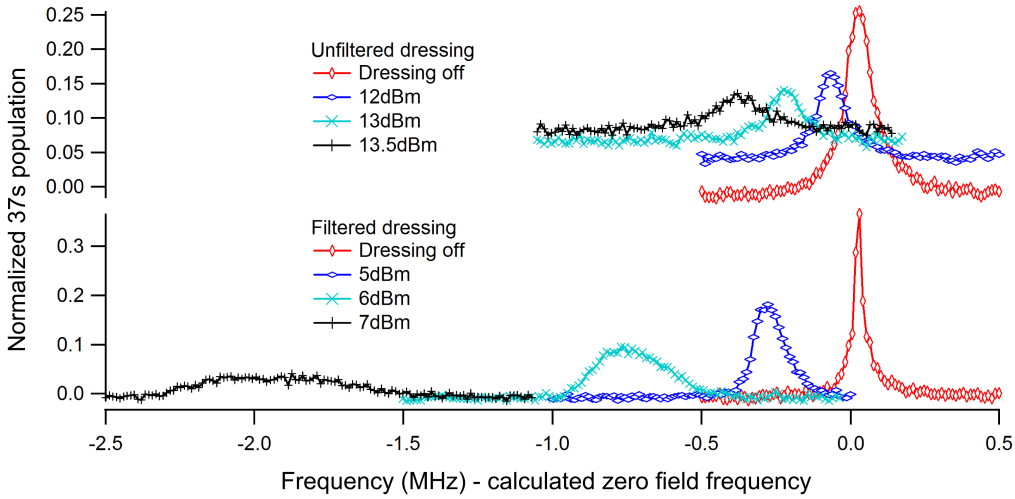

Figure 4.14: Spectral lines of the $36s_{1/2}$ and $37s_{1/2}$ transition under the influence of a 98.14 GHz microwave field, filtered by a two element tuneable split block iris filter.

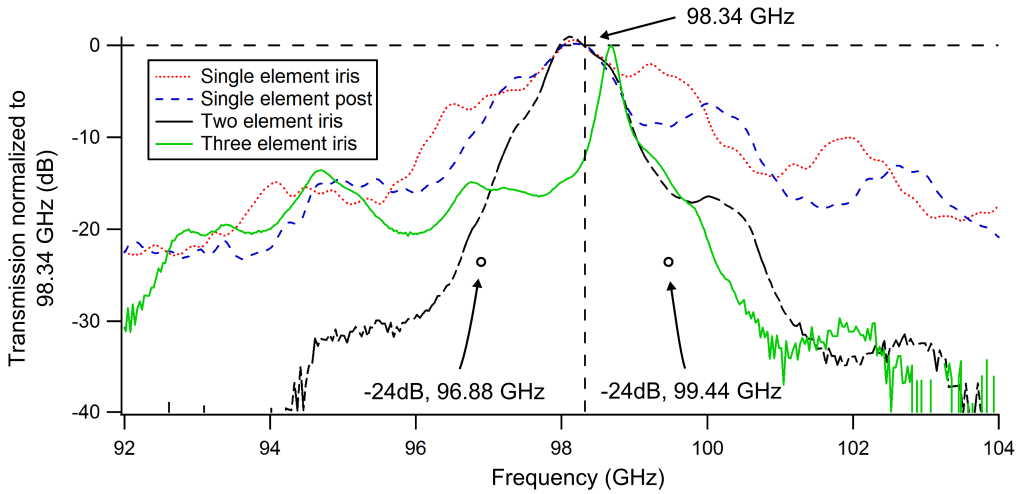

Figure 4.15: Attenuation for several filter designs. At least -24 dB of attenuation is required at the nearest atomic transition frequencies to perform the experiment.

dipole nulling experiment. As yet, this hasn't been achieved due to unreliable results when machining thin irises. Future work should be done to investigate the effect of increasing the thickness of the irises, and if this is practical, adding more elements to the filter to improve the stop-band attenuation.

Chapter 5

Conclusions

5.1 Future work

We have successfully eliminated the dipole moment difference between two states in the presence of a static electric field. This was done for one spectral line in the split $49s_{1/2} \rightarrow 48s_{1/2}$ spectrum. We believe the splitting is caused by microwave ellipticity.

Developing microwave filters would allow us to perform this experiment using a larger range of principle quantum number Rydberg states. Fabricating a three element split-block iris filter should make this possible.

An orthogonal mode coupler and phase shifter could be used to check whether the spectral line splitting is due to ellipticity in the dressing microwaves field. If the hypothesis is correct, then the dipole difference nulling experiment can then be performed in the absence of spectral line splitting.

Lastly, it would be interesting to perform coherence time measurements to determine whether this method would be useful in preserving qubits. This work could be used along with a cold atom trapping system to hold quantum information in the form of Rydberg atom qubits. Ideally these would be circular states to take advantage of the extremely long coherence times.

Bibliography

[1] P. Bohlouli-Zanjani, J. A. Petrus, and J. D. D. Martin. Enhancement of Rydberg atom interactions using ac Stark shifts. *Phys. Rev. Lett.*, 98:203005, May 2007.

[2] T F Gallagher. Rydberg atoms. *Rep. Prog. Phys.*, 51(2):143, 1988.

[3] J. Hare, M. Gross, and P. Goy. Circular atoms prepared by a new method of crossed electric and magnetic fields. *Phys. Rev. Lett.*, 61:1938–1941, Oct 1988.

[4] Randall G. Hulet and Daniel Kleppner. Rydberg atoms in "circular" states. *Phys. Rev. Lett.*, 51:1430–1433, Oct 1983.

[5] P. Hyafil, J. Mozley, A. Perrin, J. Tailleur, G. Nogues, M. Brune, J. M. Raimond, and S. Haroche. Coherence-preserving trap architecture for long-term control of giant Ryberg atoms. *Phys. Rev. Lett.*, 93:103001, Sep 2004.

[6] Newfocus Inc. FM spectroscopy with tunable diode lasers. Website, 2008. `http://www.newfocus.com`.

[7] Landau and Lifshitz. *Quantum mechanics*. Butterworth-Heinemann, Oxford, 1958.

[8] C. E. Liekhus-Schmaltz, R. Mantifel, M. Torabifard, I. B. Burgess, and J. D. D. Martin. Injection-locked diode laser current modulation for Pound-Drever-Hall frequency stabilization using transfer cavities. *J. Opt. Soc. Am. B*, 29(6):1394–1398, Jun 2012.

[9] G. Matthaei, L. Young, and E.M.T. Jones. *Microwave filters, impedance-matching networks, and coupling structures*. Artech House, Inc. Norwood MA, 1980.

[10] H. J. Metcalf and P. van der Straten. Laser cooling and trapping of atoms. *J. Opt. Soc. Am. B*, 20(5):887–908, May 2003.

[11] David M. Pozar. *Microwave engineering, second edition*. John Wiley & Sons, Inc., 1998.

[12] U. Schünemann, H. Engler, R. Grimm, M. Weidemüller, and M. Zielonkowski. Simple scheme for tunable frequency offset locking of two lasers. *Rev. Sci. Instrum.*, 70(1):242–243, 1999.

[13] Jon H. Shirley. Solution of the Schrödinger equation with a Hamiltonian periodic in time. *Phys. Rev.*, 138:B979–B987, May 1965.

[14] R.F. Stebbings and F.B. Dunning. *Rydberg states of atoms and molecules*. University Press, Cambridge, 1983.

[15] Daniel Adam Steck. Rubidium 87 line data. Website, 2001. `http://steck.us/alkalidata/rubidium87numbers.pdf`.

[16] Paul Wade. Waveguide filters you can build–and tune. Website, 2008. `http://www.w1ghz.org/filter/Waveguide_Filters_You_Can_build.pdf`.

[17] Myron L. Zimmerman, Michael G. Littman, Michael M. Kash, and Daniel Kleppner. Stark structure of the Rydberg states of alkali-metal atoms. *Phys. Rev. A*, 20:2251–2275, Dec 1979.